Materials & Design 218 (2022) 110713

Contents lists available at ScienceDirect

Materials & Design

journal homepage: www.elsevier.com/locate/matdes

A benchmark activity on the fatigue life assessment of AlSi10Mg components manufactured by L-PBF

S. Beretta [a,*], L. Patriarca [a], M. Gargourimotlagh [a], A. Hardaker [b], D. Brackett [b], M. Salimian [c], J. Gumpinger [c], T. Ghidini [c]

[a] Politecnico di Milano, Dept. Mechanical Engineering, Via La Masa 1, I-20156 Milan, Italy
[b] The Manufacturing Technology Centre (MTC), Coventry CV7 9JU, UK
[c] ESA/ESTEC, European Space Research and Technology Center, Keplerlaan 1, NL 2200AG Noordwijk, Netherlands

HIGHLIGHTS

- A wide test campaign to compare fatigue specimens with components manufactured in AlSi10Mg by L-PBF.
- There are several issues in the trasnferrability of specimen fatigue data to components.
- A fracture-based fatigue assessment is able to obtain good life predictions.
- Fracture-based assessment considers the effects of key parameters (defect-seze, residual stresses).

GRAPHICAL ABSTRACT

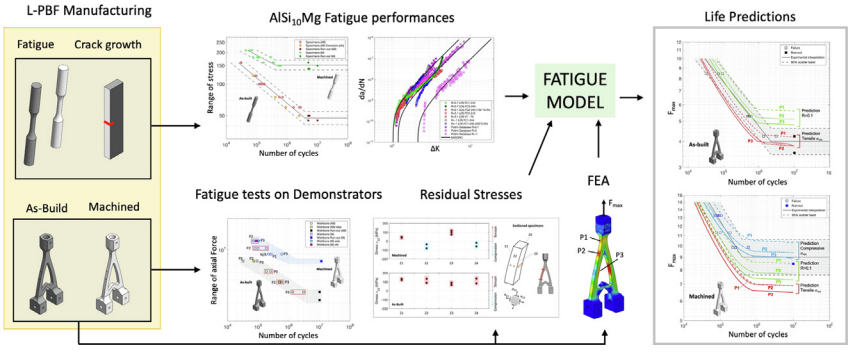

ARTICLE INFO

Article history:
Received 28 January 2022
Revised 12 April 2022
Accepted 30 April 2022
Available online 7 May 2022

Keywords:
Additive Manufacturing
Laser Powder Bed Fusion
AlSi10Mg
Defect
Fatigue propagation
Demonstrator
Assessment

ABSTRACT

One of the challenges associated with additive manufacturing (AM) is the definition of an assessment route which considers the main process signatures of the AM process. To this end, this work presents a complete benchmark activity for the assessment of an AlSi10Mg component produced by a laser powder bed fusion process, aimed at advancing the understanding of the fatigue resistance of AM materials with particular focus on the comparison between the fatigue performances of small coupons and demonstrators. Four builds of AlSi10Mg specimen geometries were manufactured to: (i) determine the fatigue curves for both as-built and machined conditions; (ii) measure the fatigue crack growth rate; (iii) produce and test under fatigue a benchmark component used as a reference for the validation of the fatigue assessment procedure. Tools and concepts of flaw tolerance were then used to perform the fatigue assessment of the benchmark component and were shown to be successful in the life prediction. Results obtained from this wide database (related to internal defects and surface features) show that only a fracture-based fatigue assessment is able to provide precise life estimates consistent with material crack growth properties. Eventually, all the experimental results including specimens design, analysis of fracture surfaces and raw tests' data will be made available in a database which can be accessed and used by the industrial and scientific communities to calibrate and validate alternative fatigue assessment procedures of AM parts.

* Corresponding author.
E-mail address: stefano.beretta@polimi.it (S. Beretta).

https://doi.org/10.1016/j.matdes.2022.110713
0264-1275/

Nomenclature

Symbols

S_y	yield stress
S_u	ultimate tensile stress
E	elastic modulus
A_u	ultimate tensile strain
A, B	equation parameters of the finite life region of the S/N diagram
$\Delta\sigma$	range of stress
$\Delta\sigma_w$	endurance limit in presence of a defect
$\Delta\sigma_{w,0}$	theoretical endurance limit for the defect-free material
σ_{res}	residual stress
$\sigma_{max}, \sigma_{min}$	maximum and minimum stresses
$\sigma_{max,eff}, \sigma_{min,eff}$	maximum and minimum effective stresses
σ_0	flow stress
ΔF	range of axial force
F_{max}	maximum axial force
$\sigma_{11}, \sigma_{22}, \sigma_{12}$	residual stress components
λ, δ	parameters of LEVD distribution
$\sqrt{area}$	Murakami's equivalent crack size
a	in-depth crack length
c	superficial crack length
N	number of cycles
R	stress ratio
R_{eff}	effective stress ratio
R_L	effective load ratio
da/dN	crack growth rate
ΔK	range of stress intensity factor
$\Delta K_{th,LC}$	range of stress intensity factor at the long crack threshold
ΔK_{th}	range of stress intensity factor at the crack threshold
K_{max}	maximum stress intensity factor
K_C	fracture toughness
ΔK_1	range of stress intensity factor at the long threshold for $R \to 1$
ΔK_1^*	range of stress intensity factor at threshold for $R \to 1$
a_0	El-Haddad parameter
$\sqrt{area_0}$	El-Haddad parameter according to the Murakami's equivalent crack size
A_0	parameter of Nasgro threshold equation
A_1	parameter of Nasgro threshold equation
A_2	parameter of Nasgro threshold equation
A_3	parameter of Nasgro threshold equation
f	crack closure factor
α	constraint factor
C_{th}^p	parameter of Nasgro threshold equation for positive R
C_{th}^m	parameter of Nasgro threshold equation for negative R
C	parameter of Nasgro equation in the Paris regime
m	parameter of Nasgro equation in the Paris regime
p	parameter of Nasgro equation in the Paris regime
R_a	mean roughness value
R_v	maximum profile valley depth
$F_{max,V}$	cumulative probability of the largest defect a in a volume V

Abbreviations

MTC	Manufacturing Technology Centre
Polimi	Politecnico di Milano
ESA/ESTEC	European Space Agency
AM	additive manufacturing
L-PBF	laser powder bed fusion
RS	residual stress
M	machined
AB	as-built
SEB	single-edge bending
WEDM	wire electric discharge machine
SEM	scanning electron microscope
CA	constant amplitude
LR	load reduction
SIF	stress intensity factor

1. Introduction

Additive manufacturing (AM), and in particular the laser-powder bed fusion (L-PBF) process, has been analysed by academia, agencies, and industry for more than two decades [1,2]. Whereas at the beginning it was considered a research field more suitable for rapid prototyping, recently it has made the step towards becoming an industrially applied process [3–9]. The intriguing possibilities of high design freedom, the possibility to fully exploit topology optimisation, the integration of different parts or the fact that no tooling is needed make this manufacturing technique particularly attractive for high-tech industries like biomedical [3], motorsports [10,11], shipbuilding [4], aviation [5] and space [6,7,9,8,12]. These benefits are the main reasons why AM has gained significant attention in the space industry. For this industrial branch, the production volumes have traditionally been low, as typically only two or maybe three parts of the same design are produced to cover development and qualification models and the flight part. Exceptions to this are commercial constellation programmes like Oneweb [13], where, as of January 2021, 110 out of more than 6000 planned satellites have been launched [14].

Certainly for aviation applications, but also for some of the space products, fatigue can be a driving factor for design. For traditionally produced materials, the fatigue behaviour has been studied for decades, and influencing factors are rather well understood [15,16]. However, it has been recognised that one of the challenges of today's L-PBF AM techniques is the rather high surface roughness and internal defects which strongly influence the fatigue performance [17–20]. The internal defects and surface roughness and surface-defects can be relieved by different post processing techniques: the hot isostatic pressing techniques for internal defects [21–23]; post-processing techniques like laser re-melting, sand blasting, chemical or electrochemical processes for surface features [24–27].

It has been recognized that the typical scatter of fatigue properties of AM materials [2] is due to the dependence of fatigue properties on the size of defects/inhomogeneities [28]. It follows that the fatigue life is strongly dependent on the position, shape and size of the so-called the killer defect [17] and it is the key ingredient for the application of the damage tolerance approach to AM products [29]. On top of that, due to the particular processing conditions of L-PBF machines, that involve melting, re-melting of the material, and constrained shrinking, high residual stresses (RSs) are typically accumulated in the produced parts [30–32]. Heat treatments applied after the AM process can effectively reduce internal stresses, but these are not expected to be removed completely [33] and can be different on witness specimens and components.

The literature on AM is rich with research works based on the experimental characterisation of conventional coupons. Few works

have focused on the manufacturing and assessment of real components [34–38], most of them concentrated on the application of traditional fatigue approaches, and some others on the porosity/defect assessment of printed parts [39–41]. However, as evidenced by A. Yadollahi and N. Shamsaei [15], changes in the size, geometry, or number of fabricated parts strongly influence the final mechanical properties of the AM part. This means that the coupons used for the characterisation might not be fully representative of the parts produced within the same build, especially for those properties related to fatigue, rather than monotonic ones [42].

It is then essential to further investigate and compare the fatigue properties of coupons and components for the sake of component qualification [43], with particular focus on the application of the assessment procedure [44] and the key features that dictate the fatigue performance such as the critical defects, the surface roughness and the RSs.

For this purpose, this work defines a comprehensive benchmark activity to assess the fatigue performances of AlSi10Mg parts produced by the L-PBF process. This study features different sample geometries and volumes (a total of 132 specimens and benchmark components tested) which were designed and tested to generate a solid material database for the implementation of the life prediction procedure. A special demonstrator was designed, tested and then used as a reference benchmark. This effort enabled to generate a big database, which can be accessed by the scientific and industrial communities for the sake of verifying different fatigue approaches and validation of fatigue assessment software (all the data generated are available through the Supplementary Material of this manuscript).

The activity described herein dealt with different phases explained in the following:

- Manufacturing of L-PBF specimens and benchmark components;
- Fatigue testing of specimens and benchmark components to provide material properties and identify the critical features (defects/surface features) at the origin of failures;
- Set-up of a fracture mechanics-based fatigue life prediction model;
- Prediction of specimens and benchmark component test results.

2. Test campaign preparation

2.1. Geometry of the specimens

The test campaign for this benchmark activity was based on AlSi10Mg manufactured by L-PBF, because this alloy has been widely adopted for AM space components [12] and its process-properties-performance has been already studied at ESA [45].

The geometry of the specimens adopted for the characterisation of the fatigue properties are reported in Fig. 1. The endurance limits and the stress versus the number of cycles to failure (S/N) diagrams were investigated according to the cylindrical geometry depicted in Fig. 1a. The gauge length of these specimens was 16 mm, while the diameter of the cross-section selected was 6 mm. The fatigue specimens were produced in two different conditions: as-built (AB) and machined (M). For the AB condition, only the two specimens' ends were machined to obtain the proper geometrical tolerances required for the fatigue tests. The machining of the M specimens was performed instead on the entire length to completely remove the external machining stock layer, which was 1.09 mm for the areas of interest (expected failures) and 0.09 mm for the attachment faces.

The single-edge bending (SEB) specimens (Fig. 1b) were designed to perform crack propagation tests under different load ratios. The nominal dimensions were 110 mm in length and with a rectangular section of 24 mm $\times$ 10.6 mm. The notch (6 mm length) was produced by means of wire electric discharge machining (WEDM) with a wire diameter equal to 100 μm: this guaranteed an initial sharp notch which favoured crack nucleation.

2.2. Geometry of the benchmark demonstrators

The benchmark components (Fig. 2) were manufactured and tested successively in the same two conditions of AB and M as the cylindrical specimens. The critical locations of failure for the AB benchmark components were characterised by the same roughness of the AB specimens, as it will be evidenced in the following. The total height of the benchmark components was 180 mm. The benchmark component was designed to have two main branches that bifurcate from the top part and are connected at the bottom part which is designed to accommodate a horizontal pin a with diameter of 7 mm. The bottom part's width was 70 mm and the thickness 30 mm. The two parts that accommodate the horizontal pin were each 20 mm thick. The top part was designed to have a threaded hole which was coaxial with the loading direction. The benchmark components were all machined in the top and bottom parts (region shaded light red, highlighted in Fig. 2) which were connected with the loading frame.

The comparison between the fatigue behaviour of cylindrical specimens and components requires the calculation of the local stresses at the failure location of the benchmark components. This calculation was done with a linear-elastic finite element (FE) model of the benchmark component. The finite elements adopted were the quadratic tetrahedral elements of type C3D10. The average dimension of the finite elements was selected to be approximately 0.5 mm in the region of the two branches and approximately 1 mm for the top and bottom ends. The total number of elements was $1.28{\cdot}10^6$ for a total number of $1.8{\cdot}10^6$ nodes. The material was modelled as linear-elastic since the yield condition was not reached in any point for the maximum applied force.

The axial force (1 kN) was applied to a reference point which was constrained to move only vertically and was kinematically coupled with the internal surface of the top part of the benchmark component (Fig. 2). In the bottom part, a second reference point was positioned in the x-y plane of symmetry and in the same position as the axis of the horizontal pins passing towards the two holes. The reference point was coupled with the two surfaces of the holes to have the same relative displacements in the Y and Z directions being free to move along X and rotate around X. Finally, the reference point was fully constrained. This allowed us to normalise the local stress values in the points of interest and simply calculate the local stresses for all the loads applied during the tests (see Section 5.3).

The benchmark components are characterized by three highly stressed regions: P1 at the neck of the upper head, P2 at the insertion of the legs onto the upper head and P3 in the middle of the legs (at the inner surface).

2.3. 3D printing and manufacturing of test pieces

All the specimens used in this study were manufactured by the UK National Centre for AM at the Manufacturing Technology Centre (MTC). L-PBF AM was used to manufacture the parts in AlSi10Mg material and the specific machine was an EOS M280 which has a build volume of 250 $\times$ 250 $\times$ 325 mm^3 (XYZ). Following a brief parameter development study the machine parameters that were found to offer the highest density levels were: power 370 W, speed 1300 mm/s, hatch distance 0.19 mm, layer thickness 30 μm, energy density 49.9 J/mm^3, and using a carbon brush recoater.

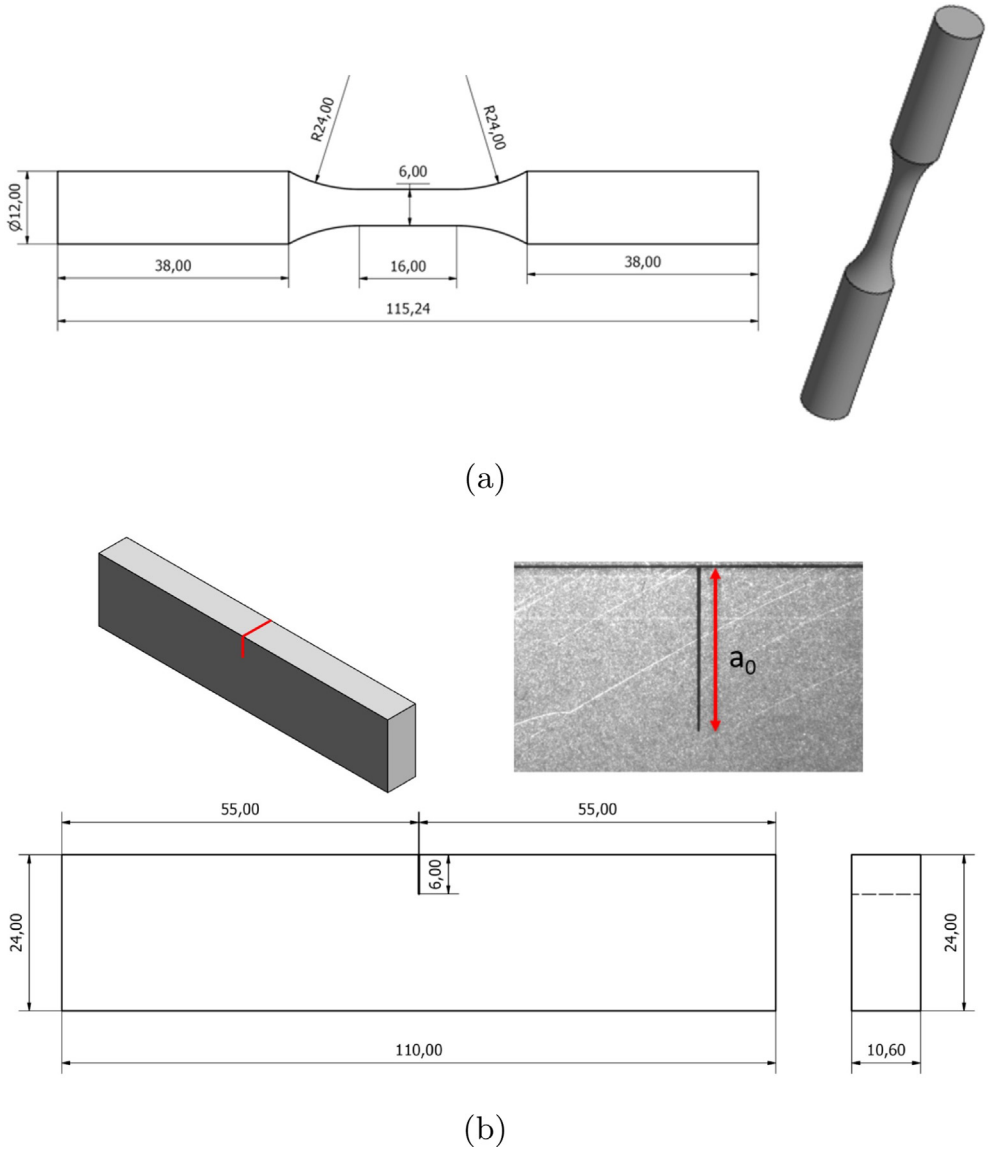

Fig. 1. Geometry of the specimens adopted in this study: (a) cylindrical specimens for fatigue characterisation; (b) the SEB specimen for fatigue crack growth characterisation.

The parts listed in Table 1 were arranged as shown in Fig. 3. Four identical builds were manufactured and they are indicated as 242, 243, 244 and 245. All parts were built directly onto the build plate with only the benchmark components requiring supports. 1 mm of stock was added to the base of all benchmark components to allow the WEDM cut to remove them from the base plate.

Results of the metallurgical analysis of the 4 cubes from each build (ref HC-X) to measure porosity are shown in Table 2 and give an indication of the material quality of the built components. The processing of the machine is shown to be relatively stable across all builds with part porosities in the region of 0.1–0.2% which is in-line with expectations from the parameter development work.

The built samples were cut off the build plate by WEDM and the parts were cleaned in an ultrasonic bath and rinsed with isopropanol to ensure they were not stored while wet. As a final check, before passing the benchmark components on to machining, one of each part type was optically scanned to ensure there was enough stock material to machine back to the final state.

2.4. Machining of the benchmark components

All benchmark components were machined in the AB condition without any heat treatment to relieve RSs. This lack of heat treatment increased the risk of deformation during the machining process which took a significant number of iterations to achieve the required tolerances. The central surfaces of the benchmark components were machined in one single operation without using a conventional strategy consisting of roughing, semi-finishing and finishing as this was also found to reduce distortion during the machining. This method also allowed access so that both sides of the benchmark component could be machined in the same operation, eliminating the need to attempt to account for distortion when flipping the benchmark component to machine the opposite face. A final roughness for the M specimens of R_a <0.8 μm was reached. The AB benchmark components were also partially machined following a similar procedure but with the first stage omitted and more attention paid to mounting the part given the increased surface roughness in the central region, which meant tolerances had to be relaxed.

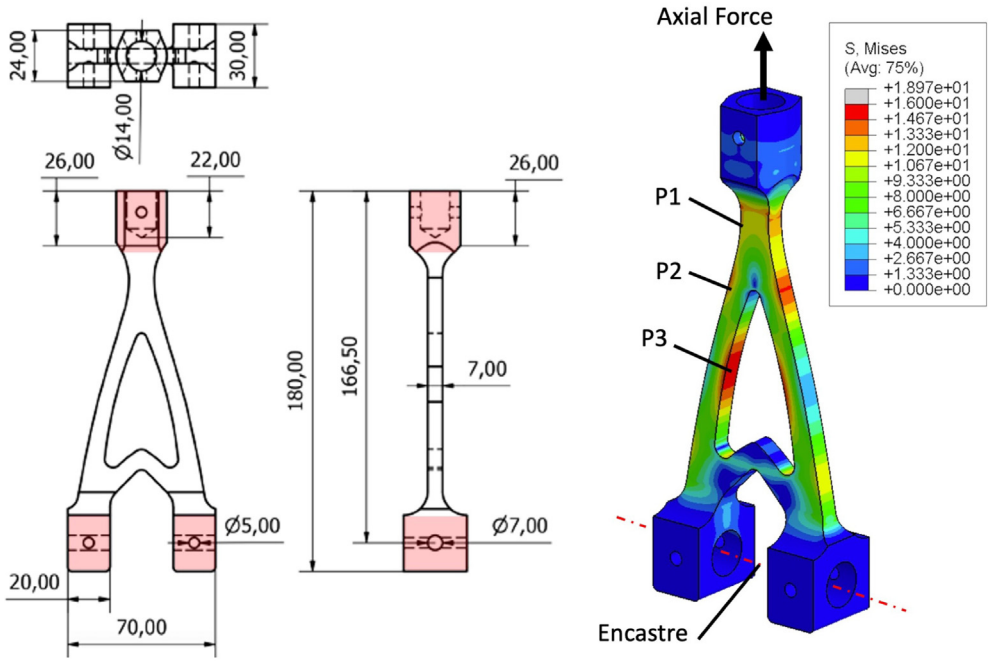

Fig. 2. The component geometry for the benchmark activity.

Table 1
Full list of components per build.

Part Name	Part Label	Quantity
Benchmark component fully machined	BM 1–4	4
Benchmark component partially machined	BN 1–4	4
Fatigue specimen fully machined	FM 1–7	7
Fatigue specimen partially machined	FN 1–7	7
Tensile specimen	T 1–4	4
Fatigue crack growth specimens	FCG 1–3	3
Metallurgy carrier samples	HC 1–4	4

3. Material and experiments

3.1. Material and microstructure

AlSi10Mg is surely one of the most adopted metal alloys for L-PBF [46]. AlSi10Mg is also used in traditional casting processes where, due to slow cooling conditions, the solid solution of silicon in aluminium is transformed into an aluminium–silicon eutectic microstructure with dispersed primary α-Al [47]. The morphology of AlSi10Mg obtained through L-PBF processes with the inherently high melting and cooling rates is significantly different and can be described with macro- and micro-structural features. The microstructure of AM AlSi10Mg is mainly driven by the applied scanning strategy [47]. For this alloy, the applied scanning strategy is characterised by rotations between layers of 67 degrees. Accordingly, the majority of melt pool boundaries on a vertical plane are elliptically shaped, whereas longitudinally shaped boundaries can be seen on horizontal planes. AlSi10Mg can precipitate Mg2Si particles naturally or through dedicated heat treatments, which increases the strength [48]. Zhang et al. [49] describe that the specific processing conditions of L-PBF lead to a microstructure where some of the Si is dissolved in the face-centred cubic α-Al matrix, resulting in a cellular dendritic α-Al phase. Si and Mg2Si particles are assumed to precipitate in this alloy and under these processing conditions [50]. The solid solution of Si was also found to decrease the lattice constant of α-Al [49]. The cell size is in the sub-micron size range and, depending on the scanning strategy, a crystal lattice with strong anisotropy can be obtained. Strategies where the scan vectors are always kept parallel from one layer to the next can promote the formation of elongated grains at the centreline of the tracks, growing in build direction (z) over several layers. According to the authors in [51], this anisotropic crystal lattice formation can be interrupted by rotating the scan vector direction by 90 degrees for each layer. The strategy applied in this work applies a scan vector rotation of 67 degrees between layers and it is believed to interrupt the formation of long, elongated grains over several layers. Since some of the parts produced in this work were large in volume, the microstructure was characterised in different locations along the build direction to verify the homogeneity of the microstructure. Fig. 4 shows the micrographs of the melt tracks for three different positions of a failed benchmark component. The specimens for the microstructural characterization were cut from the b-c-d positions indicated in the figure where the loading was not expected to induce changes in the microstructure. The etched sections show the same features in all the observed positions providing the evidence of a uniform process towards the building direction.

3.2. Experimental planning

The experimental planning related to this wide experimental campaign is summarised in Table 3. A total of 8 SEB specimens were tested and an additional set of 5 SEB specimens from a different manufacturer (same nominal alloy) was added to further confirm the results and support the crack growth data acquired. The cylindrical specimens in the AB and M conditions were produced from the AM builts 242, 243 and 245. A total of 23 AB specimens and 17 M specimens were used to characterise the entire S/N diagram, from the endurance limit to the finite-life regions. 15 benchmark components were produced in the AB conditions and 15 in the M conditions, for a total of 30 benchmark components. It should be noted that the number of tested specimens is compliant with the ECSS standard that prescribes the determination of the entire S/N diagram with at least 20 specimens for each condition. In this study, this requirement is fulfilled for both AB and M spec-

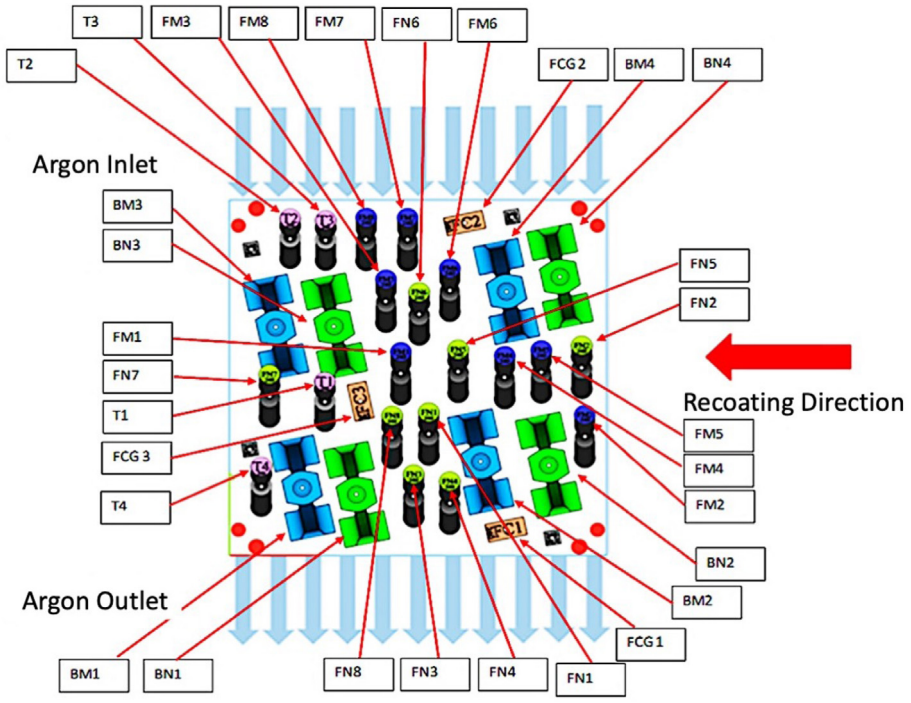

(a)

(b)

Fig. 3. (a) Image of build layout and (b) photograph of 1 of the 4 identical manufactured builds.

imen conditions considering that the run-out specimens were successively re-tested at higher stress levels (test numbers in brackets in Table 3).

3.3. Fatigue tests of cylindrical specimens

The axial fatigue tests on the cylindrical AB and M specimens were performed under a uniaxial Instron Electronpulse E10000

Table 2
Porosity measurements of the metallurgy samples in each builds.

Build Number	Sample	Porosity (%)	Mean Pore Size (μm^2)
Build 1	HC-1	0.146	59.3
	HC-2	0.133	58.1
	HC-3	0.141	54.7
	HC-4	0.106	56.0
Build 2	HC-1	0.127	61.4
	HC-2	0.172	74.7
	HC-3	0.157	66.0
	HC-4	0.144	63.7
Build 3	HC-1	0.128	60.8
	HC-2	0.144	75.2
	HC-3	0.212	74.6
	HC-4	0.176	70.8
Spare Build	HC-1	0.144	74.6
	HC-2	0.145	75.6
	HC-3	0.157	72.4
	HC-4	0.148	67.6

machine equipped with a 10 kN load cell. The tests were conducted in load amplitude control at a nominal load ratio of $R = 0.1$ and at a frequency of approximately 35 Hz. A reduction of 10% stiffness was considered as the failure condition, while the tests that reached $5{\cdot}10^6$ cycles without failure were interrupted and classified as run-outs. The run-out specimens were successively re-tested at higher load levels to feed the finite-life region of the S/N diagram. After testing, all the specimens were statically broken in two separate parts with the aim of inducing a final brittle failure through the use of liquid nitrogen to reveal and analyse the fracture surfaces. The images of the initial defects were captured with the scanning-electron microscope (SEM) at different magnifications. The aim of this investigation was to precisely locate the killer defect in terms of the following characteristics: position, shape and size. These characteristics influence the fatigue performance of the material and their quantification is important in relation to the calculation of the stress intensity factor (SIF), which is the driving force parameter selected for the characterisation of the crack propagation process.

3.4. Crack propagation tests

The crack propagation tests were performed using a resonant Rumul loading frame. The SEB specimens were subjected to a sinusoidal bending moment at a frequency of approximately 90 Hz. The crack advancement was monitored continuously by means of two alternative techniques: i) the specimen's compliance measurements or ii) surface crack measurements. A Rumul clip-on-gauge was used to detect the specimen's compliance, which depends on the crack length; this technique was adopted for positive load ratios. For negative load ratios, the measurement of the crack length was performed using two lateral resistance foils produced by Rumul (krak-gages); in this case, the change of resistance of the foils is correlated with the crack advancement. In both cases, after the tests, the specimens were broken at liquid nitrogen temperature and the final crack length was measured precisely on the fracture surfaces to correct the experimental data acquired. The correction of the crack length was effective for the calculation of the crack growth rate da/dN and for the calculation of the range of SIF ΔK. Before testing, the SEB specimens were pre-cracked to obtain an initial crack with limited load history effects, with the aim of reducing the effect of early plastic wake developed with positive pre-cracking loadings on the obtained long crack thresholds $\Delta K_{th,LC}$ [45]. The pre-cracking procedure was implemented with a load ratio of $R = -10$ and a constant ΔK=2.2 MPa$\sqrt{m}$. An average pre-crack length from 50 μm to 100 μm was measured for all the specimens.

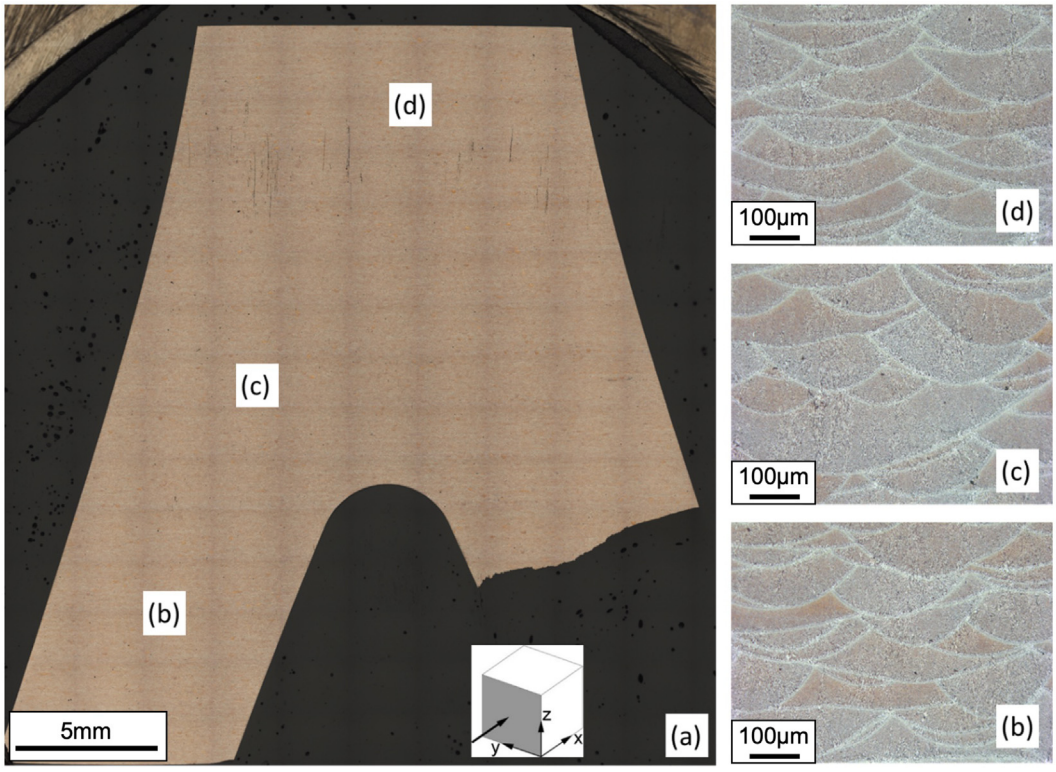

Fig. 4. Microstructure on a vertical plane of one of the benchmark components: (a) overview, indicating three areas of interest, (b) microstructure in lower area, (c) microstructure in intermediate area, (d) microstructure in upper area.

Table 3
Experimental planning of this study.

Specimen	Condition	AM build	Number of specimens
Tensile	Machined	242	4
		243	1
		244	2
		245	3
SEB	Machined	243	2
		244	3
		245	3
Cylindrical (Fatigue)	As-Built	242	8 (1)
		243	6 (1)
		245	9 (2)
Cylindrical (Fatigue)	Machined	242	5 (1)
		243	7 (2)
		245	5 (1)
Benchmark component	As-Built	242	3
		243	5 (1)
		244	2
		245	5 (1)
Benchmark component	Machined	242	3
		243	4
		244	3
		245	5 (1)

The crack propagation tests were conducted according to two different strategies: i) constant amplitude (CA), where the range of applied bending moment was kept constant for the test, leading to an increased ΔK; ii) load reduction (LR), where the range of applied bending moment was decreased to allow the applied ΔK to reach the $\Delta K_{th,LC}$. The CA is adopted to measure the crack growth rates in the so-called Paris region. The LR procedure, instead, enables us to characterise the knee-region of the crack propagation curve and the $\Delta K_{th,LC}$. It should be noted that, before starting the effective LR procedure, an initial CA procedure is also implemented to develop an initial plastic wake and stabilise the level of crack closure for the proper load ratio under investigation. The crack advancement for this initial CA step is typically 1.5 mm. Following the tests, the crack propagation rates were corrected according to the final crack length and calculated adopting a crack advancement of 50 μm.

3.5. Fatigue tests of benchmark components

The fatigue tests on the benchmark components were conducted on two different machines: (i) for the tests requiring a maximum load lower than 10 kN, an Instron ElectroPuls™ E10000 machine equipped with a 10 kN load cell was used; (ii) for the tests requiring a load higher than 10 kN, a servo-hydraulic fatigue testing system called Instron 8802 equipped with a 250 kN load cell was used. All the tests were conducted at a load ratio of R = 0.1 with a frequency of 9 Hz and 20 Hz, respectively. Those tests in which the component did not break until 10^7 cycles were considered runouts and the components were re-tested for the higher load levels. After failure, the fracture surfaces were then observed under SEM to reveal the inhomogeneities at the origin of fatigue failures.

3.6. Residual stress measurements

The RSs due to the manufacturing and machining processes were measured for the cylindrical fatigue specimens in different locations for both the AB and M conditions. In addition, a total of five crack propagation SEB specimens were also analysed. For all these specimens, the RS measurements were carried out by means of an AST X-Stress 3000 portable X-ray diffractometer using the $\sin(\phi)^2$ method. Two specimens were chosen from the AB and M series. The RS measurements were taken in the mid axial length of the specimens in four different locations along the circumference at the center. The longitudinal component (parallel to the specimen axis) of RSs was calculated.

The RS measurements for the benchmark components were performed by means of a Bruker D8 Discover diffractometer equipped with VANTEC-500 area detector with a Cu-Kα radiation at 40 kV and 50 μA and a 1 mm collimator size. The lattice strain of 422 and 420 lattice planes at 2Θ = 116.56° and 2Θ= 137.46° were measured on different points of each component. The measurements were performed on different Ψ angles from −45° to 45°. The Leptos software was used to calculate the RSs using sliding gravity and a biaxial shear stress model.

3.7. Roughness measurements

The surface roughness measurements on AB cylindrical fatigue and benchmark components were carried out using a Keyence VK-X1000 Confocal Microscope (Keyence Corporation, Osaka, Japan) at 15X magnification. The roughness measurements for cylindrical fatigue specimens were done on 4 areas centred in the gauge length on the surface with a 90 degree orientation towards each other. The same measurements were implemented for the benchmark components close to the fracture surface area of the failed part. The following steps were taken into consideration while measuring the surface parameters:

- Cylindrical specimens: three measurements with lengths of 5.6 mm were taken in the vicinity of crack initiation sites as shown in Fig. 5a.
- Benchmark components: a side surface(s) corresponding to the crack initiation site was chosen for surface evaluation. Three measurements with lengths of 5.6 mm were taken (Fig. 5b). In case of a corner crack, four measurements (two measurements on each side) were taken as shown in Fig. 5b.
- Maximum R_t and R_v values of all measurements for each specimen or benchmark component were considered for further analysis.

4. Results

4.1. Tensile properties

The tensile tests were conducted on cylindrical specimens with a nominal diameter of 6 mm according the ASTM E8/E8M-21 standard [52] that prescribes a strain rate of approximately 0.015 mm/mm/min. The number of tests was 10, as also indicated in Table 3. The tensile properties of the present AlSi10Mg alloy are summarised in Table 4, where both mean values and standard deviations are given. The mean elastic modulus was measured to be E = 69492 MPa. The yield stress S_y=258.4 MPa was determined as the proof stress for a nominal plastic deformation of 0.2%. The ultimate tensile stress was S_u=469.1 MPa and, similar to the yield stress, shows a very low scatter. The elongation at fracture was A = 8.34%.

4.2. Fatigue tests on cylindrical specimens

Fig. 6 considers a comprehensive overview of the test results obtained on the AB and M cylindrical specimens tested under constant amplitude fatigue cycles at load ratio R = 0.1. The number of repetitions of the specific combination of specimen type (AB versus M) and $\Delta\sigma$ was chosen to be approximately 3 with some exceptions for the endurance limit region where the lowest stress range was repeated only with two tests. The continuum solid lines were

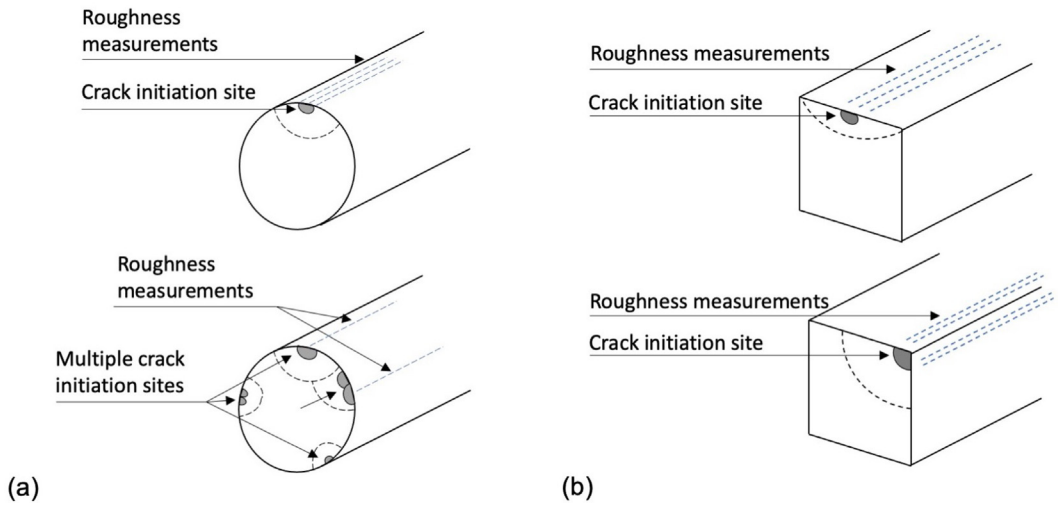

Fig. 5. Roughness measurements: position of the roughness measurements for the (a) cylindrical and (b) benchmark components.

Table 4
AlSi10Mg properties (mean and standard deviation values) obtained from the tensile tests.

Property	Mean	Standard deviation
Ultimate Tensile Stress (S_u)	469.1 MPa	1.5 MPa
Yield Stress (S_y)	258.4 MPa	3.8 MPa
Elastic Modulus (E)	69492 MPa	1511 MPa
Elongation at fracture (A_u)	8.34 %	0.46 %

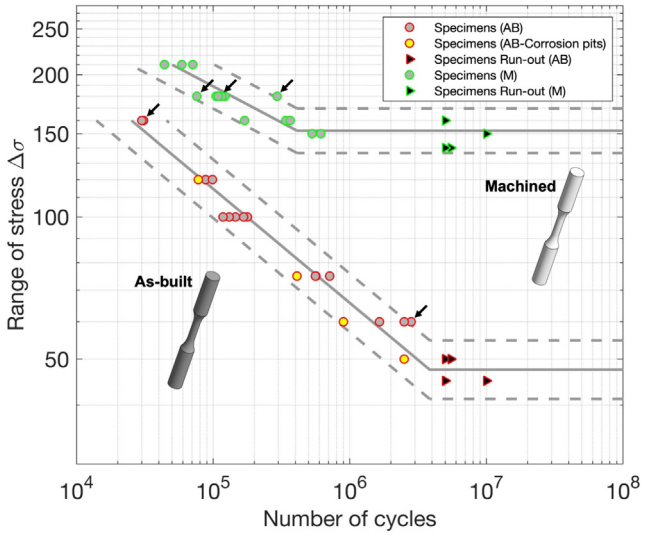

Fig. 6. S/N diagram for the cylindrical specimens, arrows indicate specimens retested at high $\Delta\sigma$ after run-out condition.

defined according to the interpolation of the failures with the equation of the type $N = A \cdot (\Delta S)^B$ by means of the least square method (see ASTM-E739 standard [53]). The endurance limits $\Delta\sigma_w^{AB}$ and $\Delta\sigma_w^M$ were calculated instead by applying the Dixon up and down method for this case of short staircase sequence [54].

One important thing to note from the results contained in Fig. 6 relates to the evidence of a sub-category of the results pertaining to the AB condition. As will be shown subsequently, some of the AB specimens (yellow dots in the S/N diagram of Fig. 6) were characterised by the presence of superficial corrosion pits. In between the AB specimen tests, those specimens characterised by these corrosion pits displayed a systematic lower fatigue life. For this reason, the analysis of this data is provided considering the separate cases of including and excluding those four data points. The fatigue tests performed on the AB and M specimens and summarised in Fig. 6 clearly indicate a strong influence on the fatigue performances of the AB condition which is also relevant when analysing the parameters of the fitted type in bi-logarithmic scale $log(N) = log(A) + B \cdot log(\Delta S)$ and the endurance limits $\Delta\sigma_w^{AB}$ and $\Delta\sigma_w^M$, see Table 5.

The typical defects detected from the fracture surfaces are depicted in Fig. 7. The fatigue strength of M specimens was controlled by the presence of small defects and pores close to the surface. For AB specimens failures were triggered by the presence of the surface features observed on net-shape surfaces. The SEM results show that, while all the cracks were initiated from the surface, the types of defects are considerably different:

- Semi-circular defects: pores and trapped particles appear as defects with equal depth to length ratio which were observed more frequently on the surface of M specimens. These defects, which occurred prior to machining the surface, were below the surface and brought to the surface by the process of machining (Fig. 7a-b).
- Elongated defects: this type of defect is characterised by a low depth to length ratio and observed over the circumference of a specimen which is a combination of defect clusters and surface valleys. This type of defect was mostly present in AB specimens and led to several crack initiation sites (Fig. 7c-d).
- Corrosion pits: this type of defect was observed on a few specimens and is characterised by a relatively large defect area and a high percentage of oxygen (in the vicinity of a corrosion pit) with respect to the other types of defects (Fig. 7e-f). Interestingly, only the specimens manufactured from AM build 242 were characterised by corrosion pits. This was also confirmed

Table 5
Summary of the fatigue properties of the present AlSi10Mg alloy in the AB and M conditions.

Condition	$log(A)$	B	$\Delta\sigma_w$ (MPa)
As-build (all)	13.53	-4.09	48
As-built (excluding corrosion pits)	14.25	-4.47	55
Machined	19.90	-6.54	152

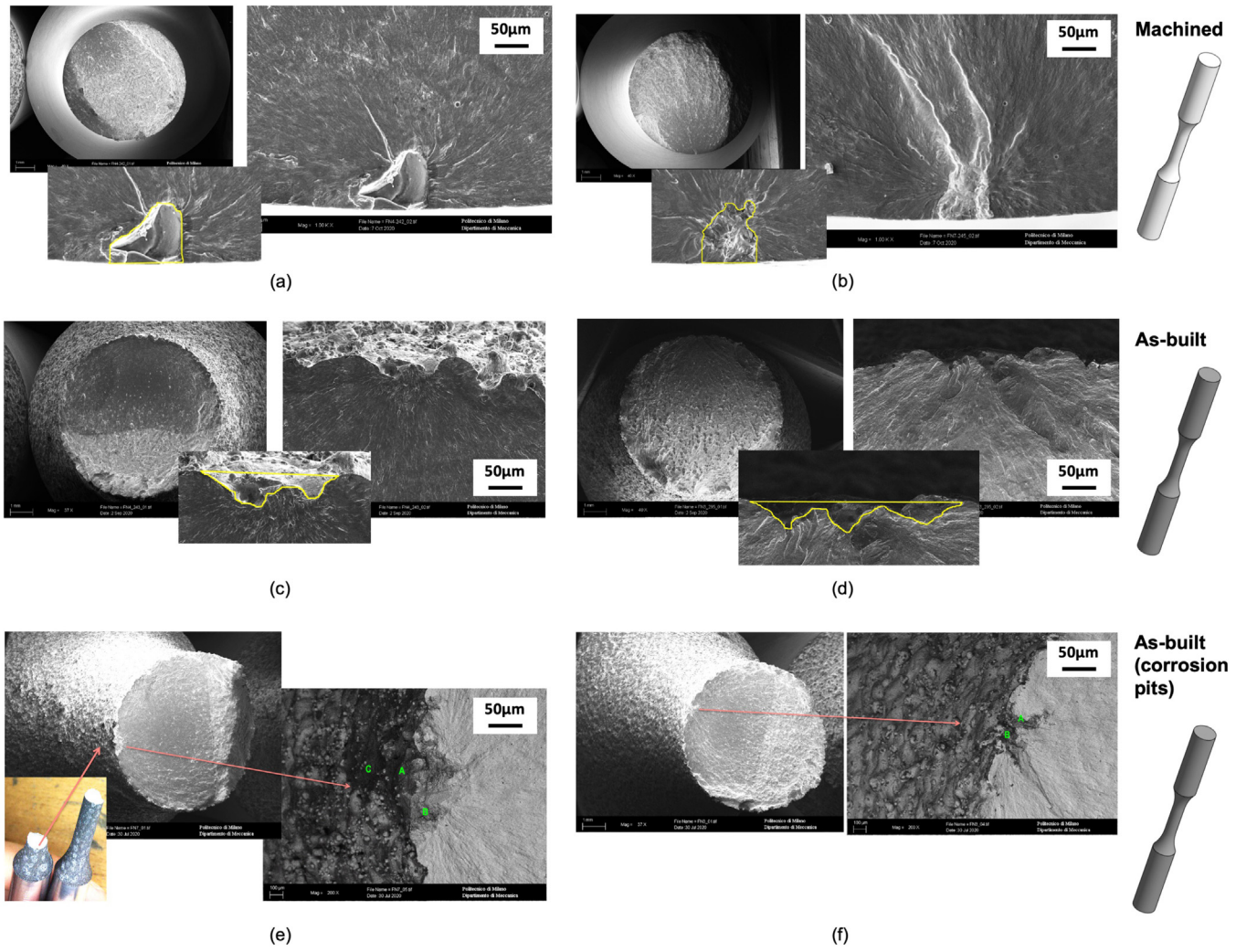

Fig. 7. Defects detected on the cylindrical specimens: (a) and (b) show two examples of defects detected from the M specimens; (c) and (d) for the AB specimens, while (e) and (f) show the origin of failure for the AB specimens which were observed to denote corrosion pits on the surface.

by the high content of oxygen (between 25% to 50%) detected in the proximity of these defects (points indicated with A, B and C in Fig. 7e-f).

4.3. Residual stresses on cylindrical specimens

Table 6 reports surface RS measurements for two AB and M specimens in terms of average of the 4 measurements with the amximum deviations. The results show tensile and compressive stresses for AB and M specimens, respectively. The presence of tensile stresses of AB specimens is due to the combination of two factors: the temperature gradients in the AM process and the cooling down phase of the molten top layers [55]. On the other hand, for the M specimens, the machining process lead to compressive RSs [56].

The values here obtained are in good agreement with X-ray measurement by Sausto on AlSi10Mg specimens [57].

Table 6
Average surface RS results of AB and M specimens in four different positions.

Specimens	S_{res} (MPa)	**Deviation** (MPa)
M cylindrical	-76	9.4
AB cylindrical	56	14.9

4.4. Crack propagation tests

The data acquired on the SEB specimens show that the crack growth rate correlates with the crack driving force parameter ΔK under the assumption of linear elastic fracture mechanics. The long crack SIF threshold ΔK_{th} values are reported in Fig. 8a as a function of the load ratio R. The data acquired from the current AM builds are indicated with the circular solid black dots (labelled with ESA in the legend). The data were then integrated with additional ΔK_{th} values from the PoliMi database characterised by the same nominal alloy composition and the same printing direction [58]. These data points are indicated with the square blue symbols and they integrate the data obtained from the current AM builds. The two databases considered were used successively to fit the NASGRO equation for the long thresholds which is indicated in Fig. 8a with a solid red continuum line. The equations used to fit the ΔK_{th} values are as follows:

$$f = max\left(R, A_0 + A_1 R + A_2 R^2 + A_3 R^3\right) \qquad R \geqslant 0 \tag{1}$$

$$\Delta K_{th} = \Delta K_1^* \frac{\left[\frac{1-R}{1-f}\right]^{\left(1+RC_{th}^p\right)}}{(1-A_0)^{(1-R)C_{th}^p}}$$

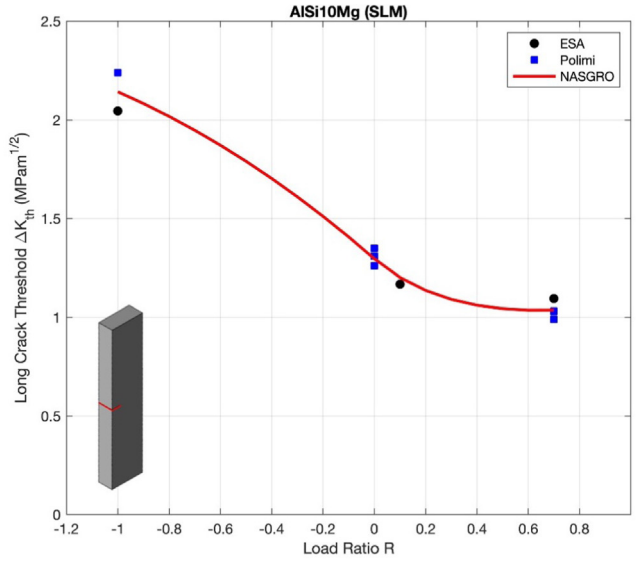

(a)

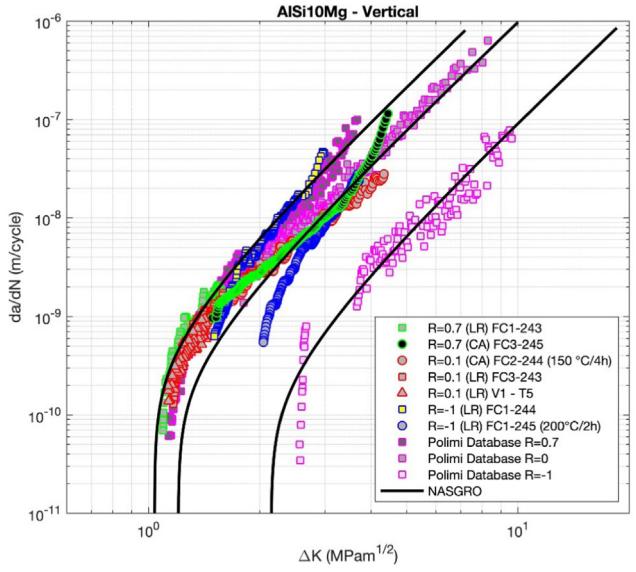

(b)

Fig. 8. Crack propagation results and their fitting with the NASGRO equation: (a) long crack thresholds; (b) crack propagation curves. The results combine two batches from different manufacturers.

$$f = A_0 + A_1 R$$

$$\Delta K_{th} = \Delta K_1^* \frac{\left[\frac{1-R}{1-f}\right]^{(1+RC_{th}^m)}}{(1-A_0)^{(C_{th}^p - RC_{th}^m)}} \quad R < 0 \tag{2}$$

$$\Delta K_1^* = \Delta K_1 \sqrt{\frac{a}{a+a_0}} \tag{3}$$

In these equations, the small crack parameter was set to $a_0 = 27.7\mu m$ while the fitting parameters were $\Delta K_1, C_{th}^p$ and C_{th}^m. The values of f and $A_{0,1,2,3}$ are provided instead with the following equations:

$$\begin{aligned} A_0 &= (0.825 - 0.34\alpha + 0.05\alpha^2)\left(cos\left(\tfrac{\pi}{2}\tfrac{\sigma_{max}}{\sigma_0}\right)\right)^{1/\alpha} \\ A_1 &= (0.415 - 0.071\alpha)\tfrac{\sigma_{max}}{\sigma_0} \\ A_3 &= 2A_0 + A_1 - 1 \\ A_2 &= 1 - A_0 - A_1 - A_3 \end{aligned} \tag{4}$$

The constraint factor α = 1.9 considers the condition of dominant plain strain for the threshold test and the ratio between the maximum stress and the flow stress is herein considered to be constant and equal to σ_{max}/σ_0=0.3.

The data points indicated in Fig. 8b show an evident effect of the RSs for the AB specimens. In particular, it can be noted that the specimens FC1-243 (R = 0.7), FC3-243 (R = 0.1) and FC1-244 (R = −1) almost overlap despite the different load ratio. This result clearly demonstrates the high level of RSs. It is also expected that, with crack propagation, these stresses tend to relax, and this further complicates the proper measurements of the crack propagation curves for the specific load ratio under investigation. For this reason, we implemented some heat treatments as indicated in the legend of Fig. 8b. The solid black continuum lines indicate the correspondence with the NASGRO equation considering all the crack growth data shown in the plot:

$$\frac{da}{dN} = C\left[\left(\frac{1-f}{1-R}\right)\right]^n \frac{\left(1-\frac{\Delta K_{th}}{\Delta K}\right)^p}{\left(1-\frac{K_{max}}{K_C}\right)^q} \tag{5}$$

The parameters C, n and p are obtained from the fitting of the experimental data (Table 7), while the parameter q is set to zero as it corresponds to the part of the NASGRO equation that describes the unstable crack propagation that occurs when K_{max} approaches the fracture toughness K_c.

4.5. Fatigue tests on benchmark components

The fatigue tests on the M benchmark components were performed based on four load levels (Fig. 9), while the AB benchmark components were tested at five load levels. The solid dots (blue for M benchmark component and black for AB benchmark components) indicate the run-outs. It is important to remark that the benchmark component geometry was designed to have different points with similar local maximum stress levels (P1, P2 and P3), leading to failures occurring in different positions, and this was also confirmed by the failure locations reported in Fig. 9 (white-filled squared dots). The point P1 is located externally and in the neck region of the components. P2 is still located on the external side of the components and it corresponds approximately with the initial position of the bifurcation of the two branches. P3 is the internal point of the branches which is the location of the maximum local stress and will be discussed subsequently. It should be noted that the failures occurred approximately in the points indicated within a range of ±5 mm. The number of failures for each position indicates that the M benchmark components mostly fail at location P2, while the AB benchmark components fail at location P3 (Table 8). Interestingly, only one failure was observed in the neck region P1 for an M benchmark component. The supplementary material contains all the information which pertain to the precise vertical position of the failures, also considering the position towards the thickness. It should be borne in mind that one M benchmark component was out of specification (red dot), but nevertheless, its result is contained in the dispersion of the data points for the specific load level.

The defects detected on the fracture surfaces for the AB benchmark component indicate that all the failures originated from superficial or sub-superficial defects (Fig. 10a-c). In particular, some of the killer defects were observed along the side of the

Table 7
Parameters of the Nasgro equation for the present AlSi10Mg alloy; crack growth rates in m/cycle and SIF in MPa$\sqrt{m}$.

ΔK_1	C_{th}^p	C_{th}^m	a_0 (m)	C	m	p
1.0741	−0.5408	0.1240	$27.7 \cdot 10^{-6}$	$1.05 \cdot 10^{-9}$	3.51	0.66

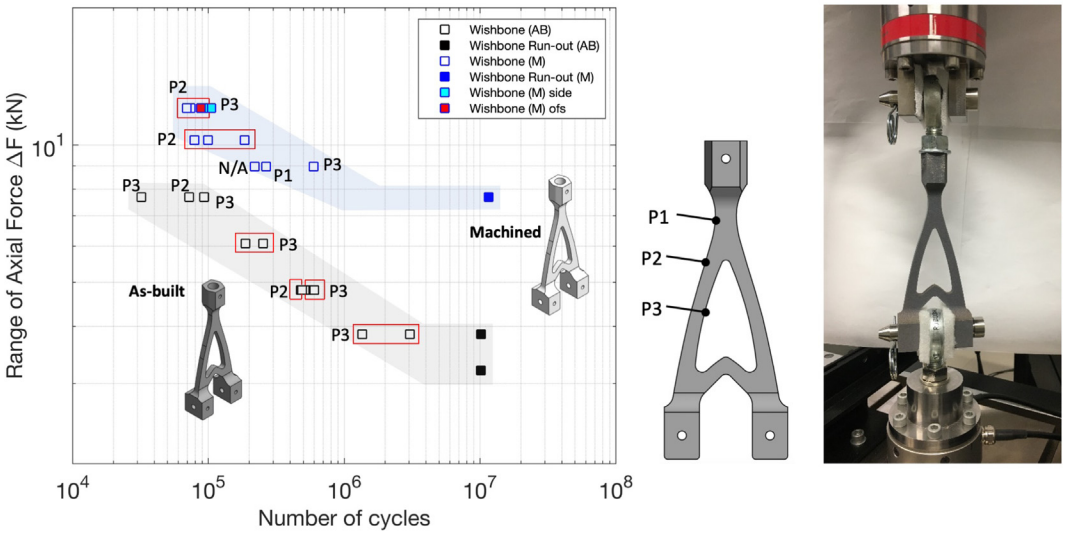

Fig. 9. Life of the M and AB benchmark components as a function of the applied load range.

Table 8
Number of failures for the locations of the M/AB benchmark components as indicated in Fig. 9.

Benchmark component	Number of failures		
	Location P1	Location P2	Location P3
Machined	1	9	2
As-built	0	3	10

cross-section (Fig. 10b-c), while failures also occurred close to the corner fillets (Fig. 10a). The failures of AB benchmark components are characterised by a different geometry of killer defects as evidenced in Fig. 10d-f. Interestingly, only AB benchmark components had a feature that could be labelled as a *corner crack* (Fig. 10d).

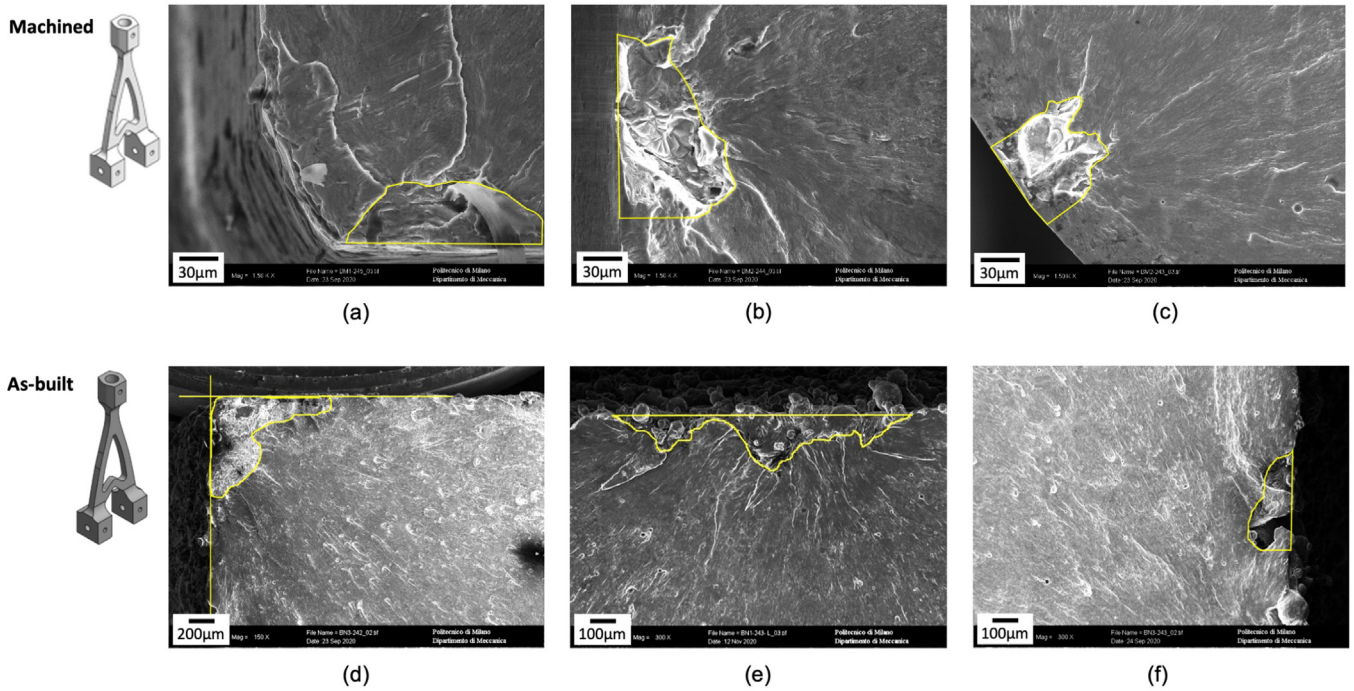

Fig. 10. Defects detected on the fracture surfaces of M and AB benchmark components.

4.6. Residual stresses on components

The RSs measurements were performed on two opposite front surfaces for two M benchmark components, namely the BM2-243 and the BM3-242 (see Tables 15 and 12 in the Appendix). For those measurements a total of 11 points for each surface was selected, as indicated in the schematic of Fig. 11a (each point represents the mean value in the specific location, and the standard deviation of those measurements is also provided in the Appendix). The locations were labelled as F1 to F5 and the normal stress σ_{22}, which is parallel to the leg axis, was analysed and plotted, as indicated in the schematic. In particular, the σ_{22} component is the stress component that was used to perform the life predictions. As for the M cylindrical specimens, for the M benchmark components all the stress measurements indicate that compressive RSs are present on the front and opposite surfaces.

Additional measurements were performed to detect the RSs on the internal and external leg sides as well, which can not be accessed when the benchmark component is not sectioned (Fig. 11b). For those measurements, one M and one AB benchmark components were selected and sectioned. Four surfaces were analysed: Z2 is the front surface (corresponding to F2 and F4 from the first measurements), Z4 is the back surface parallel to the Z2, Z1 is the external surface and Z3 is the internal surface. It is important to highlight that the machining of the Z1 and Z3 surfaces consisted of removing 1 mm in depth in one single pass initially, leaving 0.2 mm as overstock which was then removed with a final depth cut. For the lateral surfaces (Z2 and Z4), a 3 mm rough pass was adopted and followed by a final pass of 0.5 mm. For the Z2 and Z4 surfaces the RSs were measured only in two locations, while for the internal and external surfaces three points were investigated. The results are also reported in the Appendix, see Tables 16 and 17. For the M benchmark component, the RSs σ_{22} varies from approximately −80 MPa to −18 MPa in the Z2 and Z4 surfaces confirming the presence of compressive RSs. For the lateral surfaces Z1 and Z3, the RSs are observed to be positive, with values in the range of 38 to 120 MPa. These results will be extremely important for the life prediction calculations as the RS measured on the M cylindrical specimens (compressive) are different from the ones measured on the lateral sides of the M benchmark component (tensile). For all the four lateral surfaces, the M benchmark component highlights tensile RSs in the range of 65 to 138 MPa which are similar to values published for the same alloy and manufacturing process [59–61].

5. Analysis of results

5.1. Analysis of defect distributions

In order to analyse defect distributions in cylindrical specimens and components, the defects were divided into two groups based on their aspect ratios (semi-superficial length c over depth $a, c/a$). Most observed defects in M specimens/components were semi-circular pores or trapped gas (c/a=1), while the defects for AB specimens/components are rather elongated or semi-elliptical (lack of fusion, pores clusters, surface irregularities). These defects were measured in terms of Murakami's $\sqrt{area}$ parameter [62] as follows:

- for a defect with an aspect ratio, c/a <10 the $\sqrt{area}$ was calculated from the measured area of the feature at crack initiation;
- for a defect with an aspect ratio c/a >10 the effect $\sqrt{area}$ was calculated as:

$$\sqrt{area} = t_{max} \cdot \sqrt{10} \tag{6}$$

where = t_{max} is the maximum defect depth. It is important to apply Eq. 6 for wide shallow defects (c/a >10), because these defects are equivalent to a 2D edge crack and its SIF is $K = 1.12\sigma\sqrt{\pi t}$.

The defect data were interpolated with a largest extreme value distribution (LEVD) distribution and the results (LEVD parameters λ and δ together with their 95% confidence bands calculated with moment method [63]) are reported in Table 9.

Fig. 12 compares the LEVD plots adopted for defects at fracture origins of cylindrical specimens and components. It is interesting to see that for the M specimens the killer defect distributions show defects that are lower than the ones observed on components. This difference is due to the size effect, which can be explained with the different critical volume for the two test pieces [65–68] and other reasons such as the more complex geometry of the benchmark components, the altered heat flux, the solidification conditions, etc. Such an effect is not visible for the AB samples and components because the surface of the specimens is comparable with the sum of the areas of the most stressed regions of the components.

5.2. Correlation between roughness measurements and defects

The aim of this section is to evaluate the correlation between surface features (defects) and surface roughness parameters. Indeed, the method used here is based on a point-by-point comparison of $\sqrt{area}$ with R_t (maximum height of profile) or R_v (maximum depth of valley) as surface roughness representatives. The post-processing analysis to determine the maximum height R_t and lowest valley R_v was performed by MultiFileAnalyzer software (Keyence Corporation) using a multi-line roughness method. The analysis was carried out fitting the data to bi-variate gaussin distributions (BGD): the best correlation between defect and roughness data was found for R_v in terms of a log–log scale. Fig. 13c combines the results of specimen and benchmark component defect sizes versus R_v indicator together with contour levels of the BGD. The diagonal lines drawn in Fig. 13b are the approximation of the 2D crack of this type:

$$\sqrt{area} = \frac{a}{c} R_v \tag{7}$$

where a/c is the aspect ratio of a semi-elliptical crack. For an elongated shallow crack (when c/a >10), SIF can be approximated to a 2D surface crack as [62]:

$$\sqrt{area} = \sqrt{10} R_v \tag{8}$$

These lines highlight the fact that the data scatter is not only affected by defect size, but also by the aspect ratio of the defects. The central contour of BGD is intersected by the line in which $\sqrt{area}$ is approximated with an aspect ratio of a/c=0.25. This confirms the observed defects on fracture surfaces where the majority of AB defects had an aspect ratio of a/c=0.25. The upper and lower limits defined by semi-circular and elongated approximation which (in this study) are a minority among defect types.

Several studies have investigated the correlation of fatigue life data points (defect size or number of cycles to failure) with a surface representative (R_v, R_t) of AM parts: last evidences show a strong correlation with profile depth [70,70]. The expression of $\sqrt{area}$ in terms of R_v is more consistent with the concept of a 2D crack (whose *driving force* is controlled by the depth) [18], but it needs a suitable filtering of the profile [72,72]. Conversely, the assumption of R_t (or R_z) [74–77,36] would provide simple conservative estimates of defect/crack size.

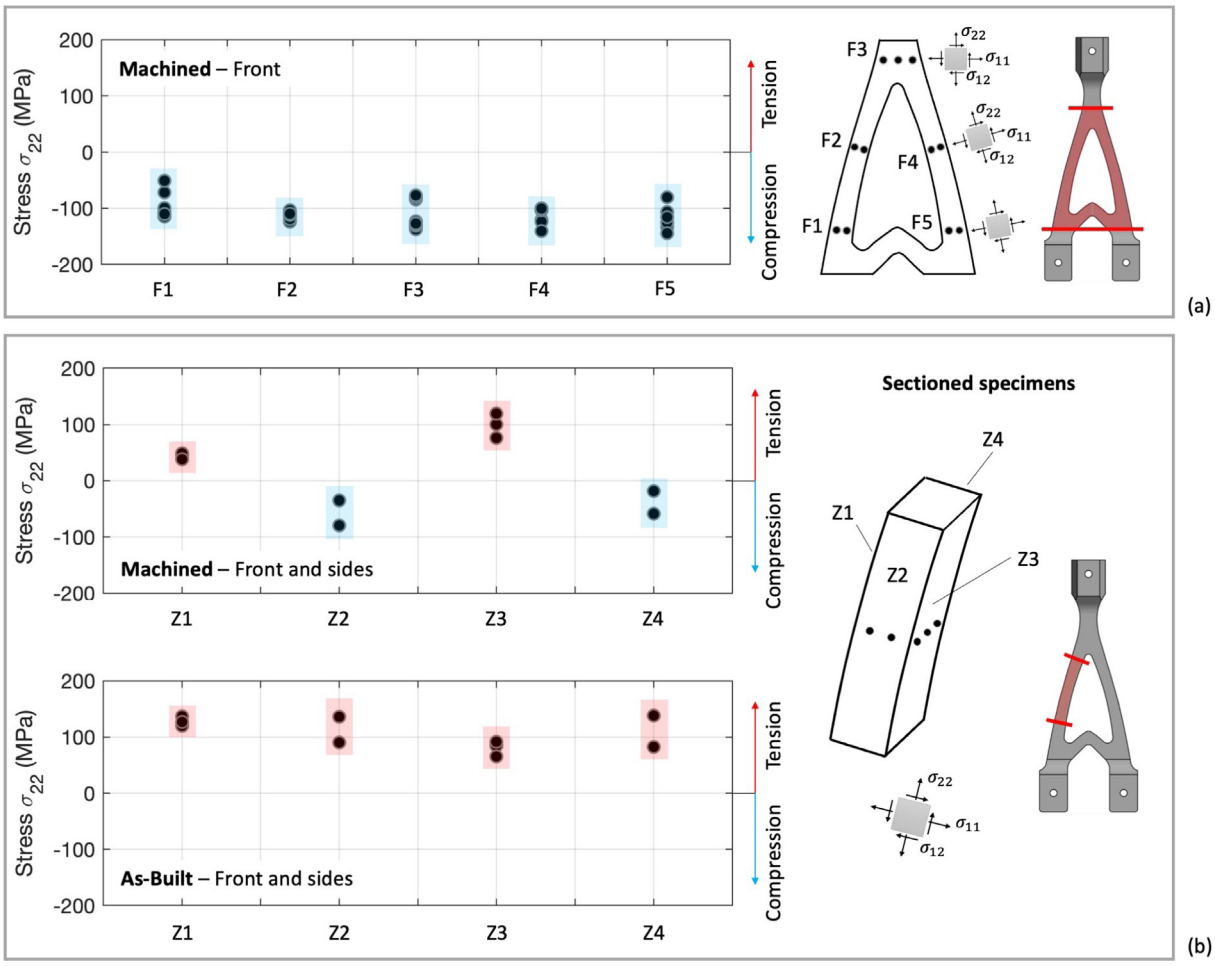

Fig. 11. RS measurements on the benchmark components: (a) front surface of two M benchmark components; (b) front and side surfaces from two pieces of benchmark component legs (M and AB, respectively); (c) in-depth RSs measured on the two points P2 and P3 for the AB benchmark component.

Table 9
LEVD parameters: comparison between AB and M specimens and components.

		λ (μm)	δ (μm)
Machined	Specimens	65.7 ± 5.1	8.3 ×/÷ 1.81
	Components	76.5± 7.1	12.1 ×/÷ 1.76
As-built	Specimens	191.0 ± 46.8	82.8 ± 60.6
	Components	210.6 ± 48.6	85.2 ± 115

5.3. Analysis of benchmark component fatigue tests in terms of local stress

Fig. 14 shows the contour plot of the maximum principal stress on the benchmark component calculated according the finite element model. Once the local state of stress was available, the experimental test data (load, failure position) on components could be processed to obtain the local stress at each failure location. The S/N diagram reported in Fig. 14 compares the results obtained from the fatigue tests on the cylindrical specimens with the results obtained from the local stress ranges on the failure location of the benchmark components. The results of the M benchmark components are very dispersed and, contrary to the results in [38], they also show a lower fatigue resistance with respect to the M cylindrical specimens. In fact, the lower fatigue resistance of the M benchmark components is related to the different killer defect distributions, as evidenced clearly in Fig. 12a (further discussion in Section 9). Moreover, the RSs in the internal and external sides of the M benchmark components are in tension (locations Z1 and Z3 in Fig. 11), while cylindrical specimens had compressive RSs. Conversely, the AB benchmark component results overlapped almost perfectly with the results on the AB cylindrical specimens. At first glance, the average dimension of the killer defect is similar for the AB cylindrical and benchmark components (Fig. 12b). However, the level of the RSs is even higher than that of the specimens. To overcome these limitations, an analysis based on fracture mechanics concepts was adopted and its comparison with a local stress approach is discussed in the following section.

6. Fracture mechanics-based life prediction

6.1. Life prediction of cylindrical specimens

It is well established that the condition of failure or run-out for loadings under fatigue for ALSi10Mg parts produced by AM is controlled by the features associated with the killer defect and the endurance limit, which is, in general, a material property that is not unique but also depends on the crack length. The El-Haddad model modified according to the Murakami approach to defects applied to the AM AlSi10Mg has been widely discussed in [19,28]; the reader is referred to these references for further details. In this framework, the relationship between the fatigue limit and the defect/crack size can be described by the following equation:

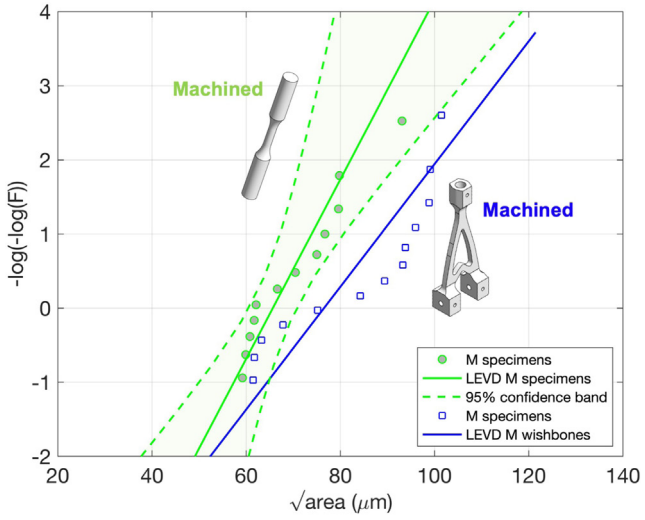

(a)

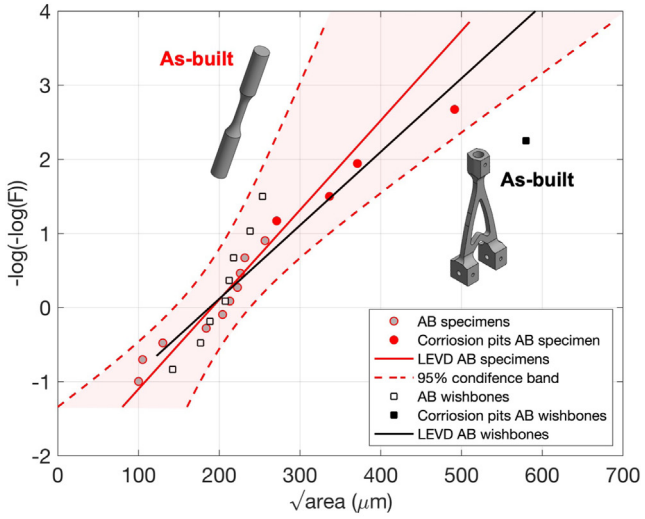

(b)

Fig. 12. Defect distributions for the (a) M and (b) AB specimens.

$$\Delta\sigma_w = \Delta\sigma_{w,0}\sqrt{\frac{\sqrt{area}}{\sqrt{area}+\sqrt{area_0}}} \tag{9}$$

where $\sqrt{area_0}$ is defined as the El-Haddad parameter which is found as the intersection point in the Kitagawa–Takahashi diagram between the theoretical endurance limit $\Delta\sigma_{w,0}$ and the line representing the endurance limit determined by the long crack threshold $\Delta K_{th,LC}$:

$$\sqrt{area_0} = \frac{1}{\pi}\left(\frac{\Delta K_{th,LC}}{Y\cdot\Delta\sigma_{w,0}}\right)^2 \tag{10}$$

The geometry factor selected was $Y = 0.65$, which can be applied to a superficial crack with the dimension defined by $\sqrt{area}$. The $\Delta K_{th,LC}$ values were obtained from the NASGRO fitting, see Fig. 8a and Table 7. To estimate the theoretical endurance limit ($\sqrt{area}\to 0$) $\Delta\sigma_{w,0}$, we used the monotonic properties (Table 1). We herein denote it as theoretical in relation to the evidence that it cannot be measured experimentally due to the unavoidable presence of defects in the fatigue specimens. The theoretical endurance limit $\Delta\sigma_{w,0}$ is then estimated from the S_u for the load ratio R=-1 according $\Delta\sigma_{w,0}^{-1} = 2\cdot(0.4\cdot S_u)$=375.3 MPa [77]. The dependence of the $\Delta\sigma_{w,0}$ on the load ratio is then defined by the Goodman model for a load ratio higher than −1:

$$\Delta\sigma_{w,0}^{>-1} = \left(\frac{1}{\Delta\sigma_{w,0}^{-1}} + \frac{1}{2\cdot S_u}\frac{1+R}{1-R}\right)^{-1} \tag{11}$$

The effective stress ratio in the absence of RSs is equal to the stress ratio applied during the test (R_L=0.1). However, as shown previously, compressive and tensile RSs are present on the surface of M and AB specimens, respectively. Whether the RSs are tensile or compressive, the effective stress ratio R_{eff} on the surface of specimens can be calculated, which is relevant for the threshold condition of surface defects based on the stress intensity factors:

$$K_{max,eff} = \frac{\Delta K}{1-R_L} + K_{res} \tag{12}$$

$$K_{min,eff} = \frac{\Delta K}{1-R_L}R_L + K_{res} \tag{13}$$

where ΔK is the range of SIF, $K_{max,eff}$ is the maximum effective SIF, $K_{min,eff}$ is the minimum effective SIF, and K_{res} is the SIF as calculated considering the average measured surface RS reported in Table 6. The calculation of the SIFs was performed according to the weight functions of Wang and Lambert for low $a/c < 1$ [78] and high $a/c > 1$ [79]. In correspondence with the endurance limit determined for the M and AB cylindrical specimens, we calculated R_{eff} which was −0.22 for the M condition and 0.56 for the AB condition. Providing these R_{eff} values, the $\Delta\sigma_{w,0}$ and $\Delta K_{th,LC}$ are then determined and used to construct the Kitagawa diagrams according to the El-Haddad model. Table 10 compares the reference case R_L= 0.1 and the calculated Kitagawa diagram parameters at R_{eff}.

The El-Haddad models are reported in Figs. 15a-b together with the experimental results obtained on the cylindrical specimens. Please note that for each load ratio, three lines are plotted which correspond to three values of theoretical endurance limit $\Delta\sigma_{w,0}$, considering a scatter of ±5% on the theoretical values estimated from the static properties. Each data point was introduced in the figure according to the size in terms of $\sqrt{area}$ and the applied stress range. For the M specimens, the effective load ratio was calculated considering that the surface RS in compression decreases to zero in a depth of 0.1 mm (as experimentally measured by Sausto et al. [57]). Under this assumption, the deepest point of the crack front determines the critical condition, for this point $R_{eff} = -0.22$ was calculated. The results evidence that the predictions performed for R = 0.1 are conservative, while for R_{eff}=-0.22, they are close to the experimental data. Similarly, also the AB results are estimated with a high level of accuracy by the El-Haddad model considering the effective load ratio R_{eff}=0.56, whereas the prediction performed withe the nominal load ratio of R = 0.1 does not match the experiments precisely. In summary, the results reported in Figs. 15a-b demonstrate that the endurance limit of the cylindrical specimens can be readily predicted by the El-Haddad model and by considering the effect of the RSs.

We now focus our attention on the prediction of the finite life region for the cylindrical specimens. The life predictions were performed considering the following assumptions:

- The initial crack size was taken as the average size of the killer defects detected on the fracture surfaces of specimens (Figs. 12-a-b).
- For the M specimens, the crack shape assumed was semi-circular with aspect ratio of approximately a/c=1 suggested by the shape of defects detected on the fracture surfaces (Figs. 7-a-b). For the AB specimens, the semi-elliptical (elongated) shape with an aspect ratio of a/c=1/2.5 was selected (Figs. 7c-d).

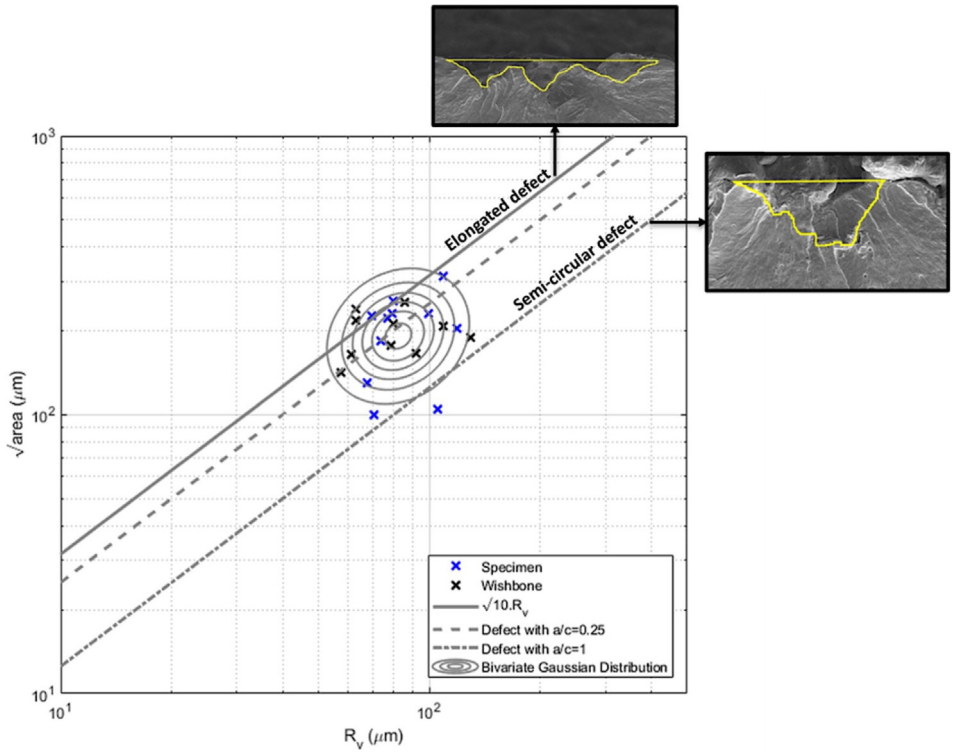

Fig. 13. Surface roughness analysis by adopting bi-variate gaussian distribution to the data set: correlation of defect size (specimens and components) versus R_v obtained by stylus.

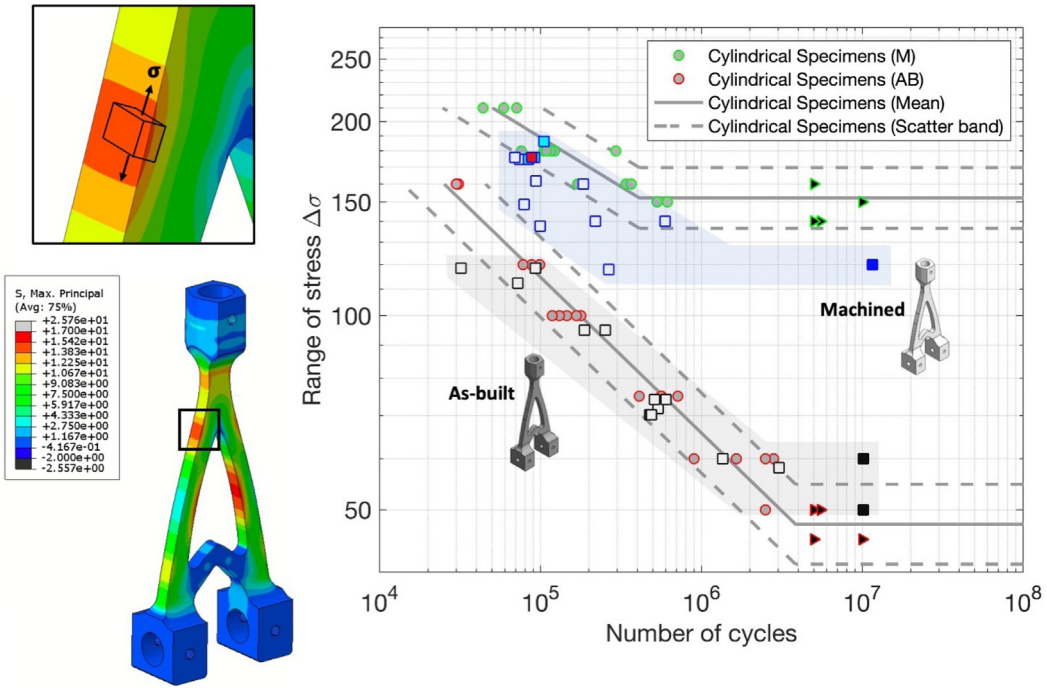

Fig. 14. S/N diagram considering the local stress range on the failure location of the components and the results of the M specimens.

- The RS profile was assumed to linearly decrease from the experimental RS value measured on the surface to zero towards a depth of 0.1 mm for M specs (as experimentally measured by Sausto et al. [57]) and 0.5 mm for AB specs, a constant stress was then assumed to balance the equilibrium over the section.
- The effect of the RSs was accounted for by a contribution (positive or negative depending on the RS profile) to the average SIFs thus changing the local effective stress ratio.
- The calculation of the SIFs was performed according to the weight functions of Wang and Lambert for low $a/c < 1$ [78] and high $a/c > 1$ [79].

Table 10
Comparison of Kitagawa diagram parameters at applied and effective stress ratios.

	Stress ratio	$\Delta K_{th,lc}$ (MPa$\sqrt{m}$)	$\Delta\sigma_{w0}$ (MPa)
Reference	$R_L = 0.1$	1.20	251.3
Machined	$R_{eff} = -0.22$ (at fatigue limit)	1.53	298.2
As-built	$R_{eff} = 0.56$ (at fatigue limit)	1.04	155.2

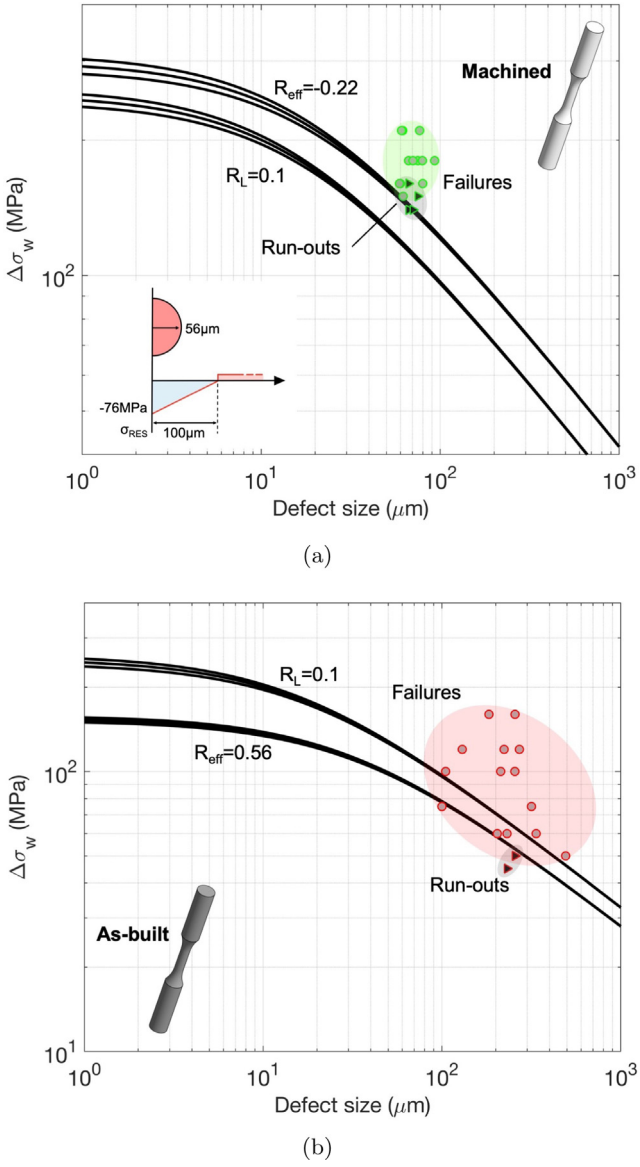

Fig. 15. Kitagawa diagrams and comparison with cylindrical specimen tests considering the effect of the RSs in the effective load ratio: (a) M specimens, (b) AB specimens.

- The crack growth model adopted is the NASGRO equation fitted on crack growth data reported in Fig. 8 and the parameter $\sqrt{area_0}$ dependent on the stress ratio [80] according the Eq. 10; the failure condition corresponded to the average crack depth at failure observed on the fracture surfaces.

Life predictions for the AB and M cylindrical are compared with the number of cycles to failure detected (see Fig. 16). The continuous grey lines refer to the interpolation of the experimental data points and the dashed lines refer to the 95% scatter bands. The predictions are indicated in the same figures with the blue and black lines. It is important to highlight that these calculations were performed at a variable R_{eff} since the RSs are constant for each stress level $\Delta\sigma$ and this dictates a variable R_{eff} which is considered in the present simulations. Additional life predictions at the nominal stress ratio R = 0.1 are also shown with black lines. The results show that for both the M and AB specimens, the crack growth simulations that consider the RSs are close to the experimental data points in both finite and infinite life regions of the S/N diagrams. On the other hand, the predictions considering the nominal stress ratio lead to a significant underestimation of the stress ranges for the M specimens and to non-conservative predictions for the AB specimens.

6.2. Life prediction of benchmark components

For the purpose of predicting the life of components, the general approach is the same as that adopted for the cylindrical specimens.

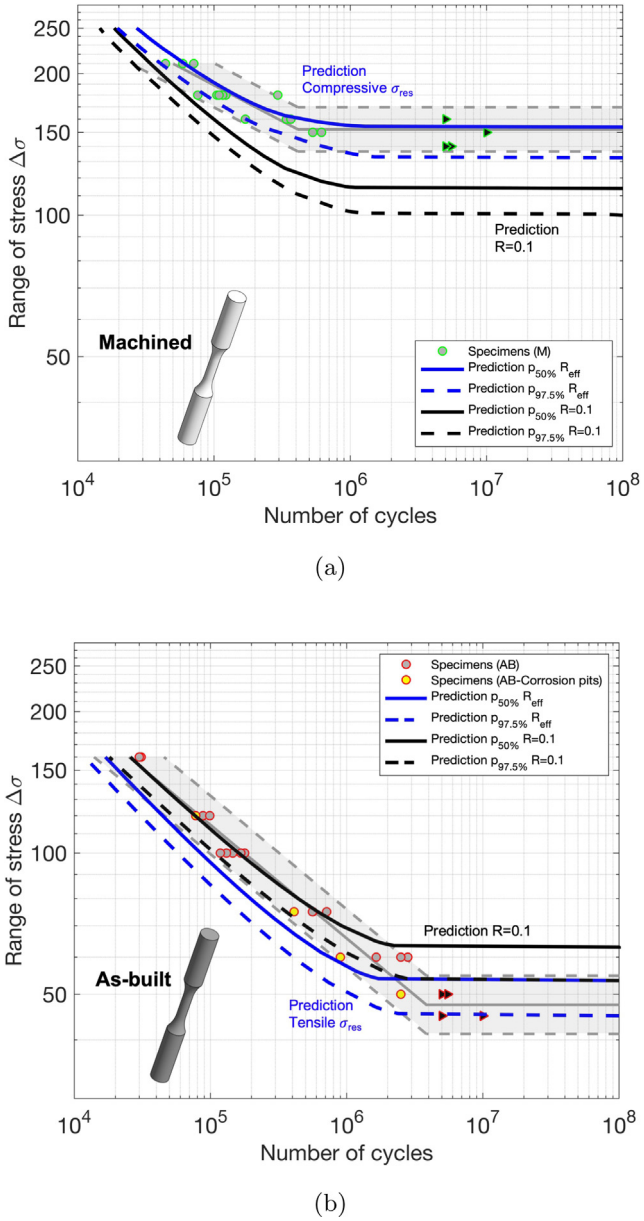

Fig. 16. Life predictions for the (a) M specimens and (b) AB specimens. The S/N diagrams were predicted considering the stress ratio as the nominal load ratio applied to the specimens and the effective stress ratio considering the measured superficial RSs.

In particular, a set of predictions were performed considering the most stressed position of the components, as calculated from the finite element simulation (P1, P2, and P3, see Fig. 14). In this regard, three life predictions will be considered which correspond to the three potential failure locations P1, P2 and P3. As for the specimens, to consider the stress gradient towards the thickness of the components, the Wang and Lambert SIF functions [79,79] were taken into consideration.

The effective stress ratio at any stress level for components was calculated by superimposing the RS profile with the stress distribution along the thickness of the above mentioned failure positions. Determine the RS profile at each failure position is time consuming and complicated, thus, a general pattern was considered for the M benchmark components in which the surface RS until the depth of 100 μm equals the measured average surface RS and linearly goes to zero through the thickness of the components. Then, the SIF was obtained by the Wang and Lambert weight function using the superimposed stress distributions. For the AB benchmark components, the stress profile was taken as the one measured experimentally (see Fig. 11c).

Figs. 17a-b show the life prediction results for the M and AB benchmark components, respectively. The life predictions were performed considering the nominal load ratio (R = 0.1, green lines). In addition, the life predictions were also performed with the effective load ratio R_{eff}, which considers the effect of the RSs, and are reported in red. As expected, the life predictions performed with R_{eff} for the AB benchmark components show a lower fatigue resistance due to the presence of tensile RSs (Fig. 11a). For the M benchmark components, the life predictions performed adopting the nominal stress ratio are slightly conservative (especially at the endurance limit region), as indicated by the green lines in Fig. 17b. It should be noted that for the M benchmark components it is more difficult to introduce the effect of the RSs as these stresses strictly depend on the failure position. In fact, Fig. 11b indicates that the two front surfaces are characterised by compressive RSs. On the other hand, the failures are mostly located on the internal (position P3) and external (position P2) sides on the components where slight tensile stresses were measured. For the life predictions, the most conservative assumption (tensile stresses) was adopted and, as highlighted in Fig. 17, this choice determined conservative life predictions. However, it should be noted that some failures were experienced at the corners where the RS pattern should be discontinuous. This is also evidenced by the fact that the life predictions adopting the nominal stress ratio are close to the experimental values. When comparing the life predictions of the three typical failure locations, it is evident that the most severe location is P3, while the predictions performed for P1 display the longest lives. If we compare the failures observed experimentally, Table 8 indicates that for the AB benchmark components, the failure position that occurs in the majority of cases is P3. The life predictions performed for P3 (continuum solid lines in Fig. 17a) are very close to the experimental values when the RSs are considered in the simulation. The failure positions observed for the M benchmark components indicate that the most critical point is P2 (Table 8). For the life predictions the difference between the curves comparing P2 and P3 can be estimated to be less than 10% in terms of predicted failure load for a specific expected life. In this case, the prediction based on point P3 would provide a reasonably conservative estimate.

7. Discussion

This study addressed the manufacturing, characterisation and fatigue assessment of AM demonstrators produced by the L-PBF process with the final aim to verify the applicability of the concepts contained in ECSS standards for the qualification of AM materials [81] and the validation of a probabilistic fatigue assessment software for components with defects [82] that will be addressed in a forthcoming paper.

The first result of this wide-ranging activity deals with the fatigue assessment of the components by adopting the fatigue properties obtained from the M and AB specimens. The two scenarios for transferability of fatigue data from specimens to components can be summarised in the schematic of Fig. 18. The simple idea that specimen data could be directly transferred to components (with a suitable multiaxial criterion as in [83]), worked well for AB benchmark components. Conversely, for M components, the analysis based on the local stresses clearly showed that fatigue properties of M benchmark components were lower than those of specimens, with approximately 15% lower fatigue limit.

To understand the factors behind this lack of direct transferability, it is worth remembering that fatigue properties of AM materials are inherently controlled by the size of manufacturing defects and that they could be modelled adopting suitable short-cracks models (i.e. models in which the crack growth properties depend on the crack size) [28,29]. Many papers have shown the success of this concept for describing fatigue properties of Al alloys [19,84,85], Ti6Al4V [76,86,87], stainless steels [89–91] and Ni-based superalloys [93–95] manufactured by AM processes.

When the problem of fatigue of AM materials is correctly addressed in terms of crack growth (or threshold for the fatigue strength) assessment, then the relevant factors (for a given material) are [96]: i) the defect/flaw size and ii) the stress ratio, which in our case is also influenced by the RSs.

7.1. Defect size and "Size effect"

Concerning the first factor, it is clear that the defects detected at the origin of fatigue failures of M benchmark components are larger than the ones detected on the M specimens. The larger critical defect observed for the benchmark components is related to the "size effect" [65–68]. Considering two different volumes V_1 and V_2, the cumulative probability of the largest defects in V_2 could be derived from [97]:

$$F_{max,V_2}(a) = \left[F_{max,V_1}(a)\right]^{V_2/V_1} \tag{14}$$

where a is the defect size. Eq. 14 indicates that the larger is the volume V_2, the larger will be the critical defect that can be found in it. Analysis of defects through Eq. 14 is the approach usually adopted for considering the *scale effect* due to internal defects in life prediction of AM materials [93,75] and processing CT-scan data [39,98,99,86,100,85].

The transformation of Eq. (16) produces, if the distribution of maximum defects in V_1 is LEVD, that largest defects on V_2 should be described by a LEVD with parameters:

$$\begin{cases} \lambda_{V_2} = \lambda_{V_1} + \delta_1 \cdot log(V_2/V_1) \\ \delta_2 = \delta_1 \end{cases} \tag{15}$$

It is possible to apply Eq. (15) considering for V_2 the 80% volume of specimens and components (the material volume in which $0.8\sigma_{max} < \sigma < \sigma_{max}$), as suggested in [82], and take the specimen volume for V_1. The confidence bands of the estimated distribution can be simply obtained from the estimates for (λ_1, δ_1) [102,63].

The application of this analysis to the distribution of defects in machined samples to estimate the distribution on M benchmark components is shown in Fig. 19a. The defects detected on the benchmark components are at the upper bound of the 95 % confidence of the estimated distribution. As it can be expected, the volume of the printed part, the inter-layer time intervals and thermal dissipation during the AM process have an influence [15], but nev-

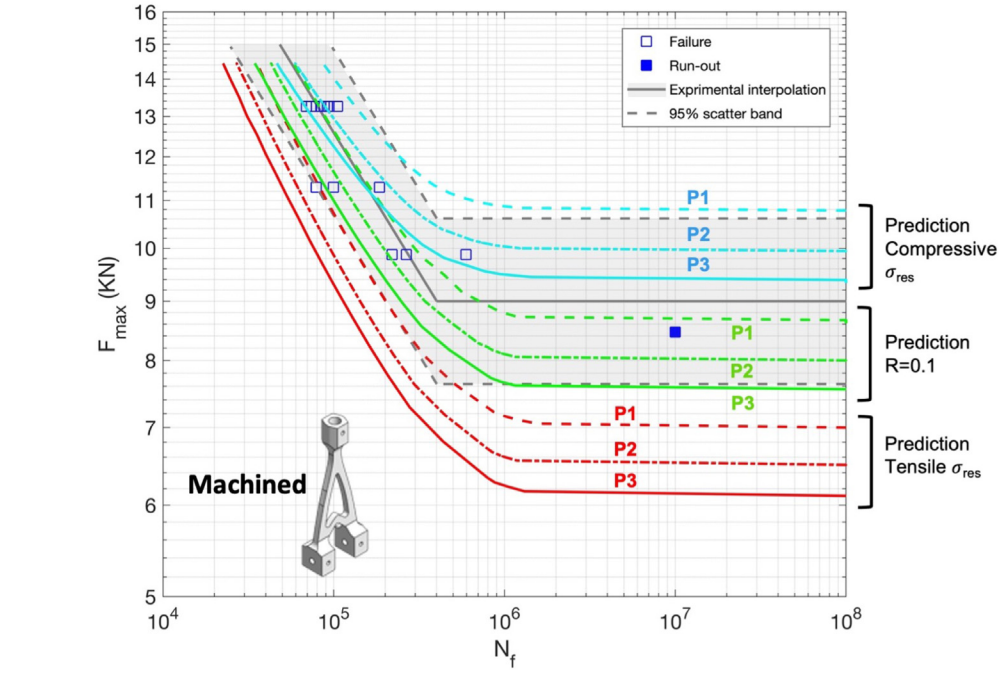

(a)

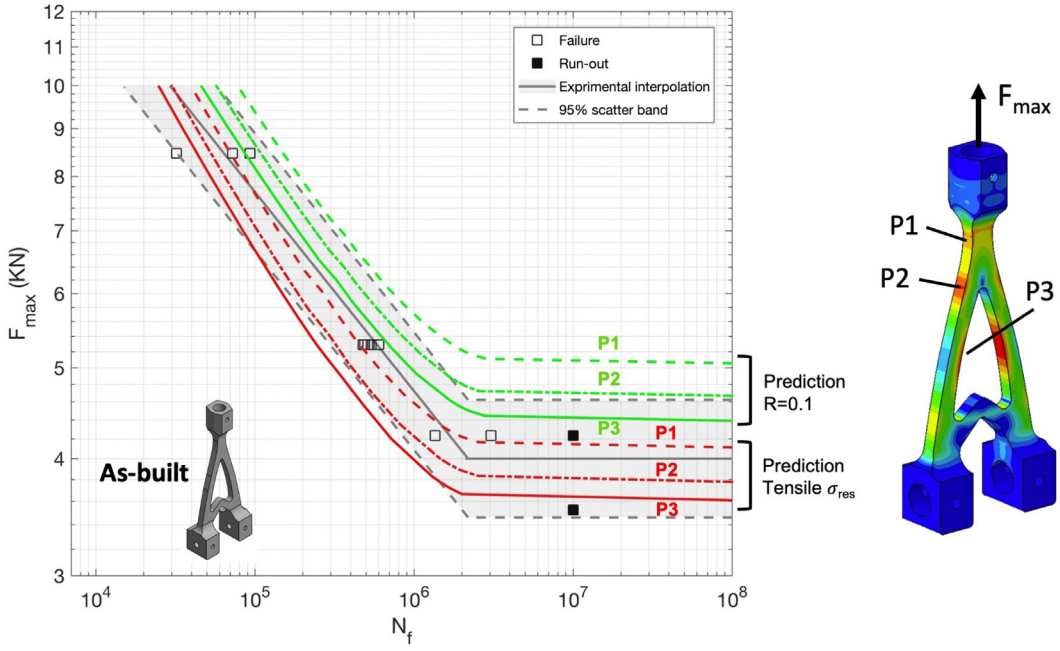

(b)

Fig. 17. Life prediction for: (a) M benchmark components, (b) AB benchmark components.

ertheless the estimates are quite good. This confirms that a suitable analysis (considering the confidence intervals of the estimated values) of fatigue specimen data can provide a first estimate of the *size effect* for a correct analysis of components. (See Table 11).

Similarly, the results of AB surface defects show that the two distributions are similar even if the most stressed region of the surface area of the components (once again defined for surface region for which $0.8\sigma_{max} < \sigma < \sigma_{max}$) is approximately twice the lateral surface of cylindrical specimens. In this case, the adoption of Eq. 14 would lead to a good estimation of defects to be considered for AB benchmark components if the data of corrosion pits would be omitted (they are not relevant for benchmark components).

7.2. Residual stresses and stress ratio

The second main factor that dictates the fatigue resistance of AM parts is the presence of RSs. The AB specimens and AB benchmark components were both characterised by tensile superficial

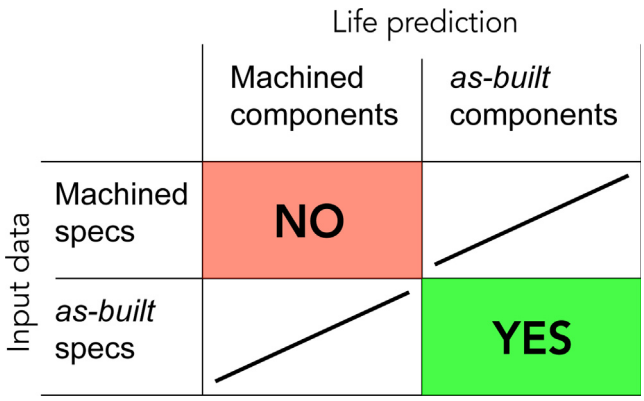

Fig. 18. Scheme of the results about transferrability of specimen fatigue tests data to components.

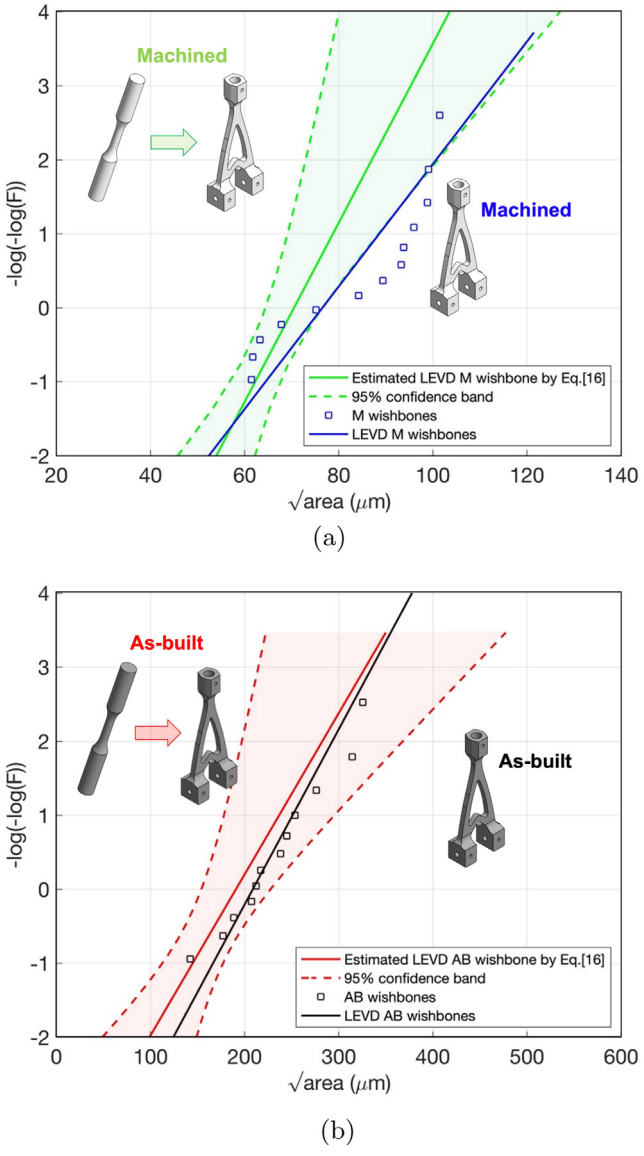

Fig. 19. Comparison between defects on benchmark components and estimates from specimen data (Eqs. (16)–(17)): (a) M benchmark components; (b) AB benchmark components (corrosion pits were excluded from the analysis because they are not relevant for demonstrators).

Table 11
Relevant surfaces and volumes for 'size effect'.

	80% Volume [mm^3]	80% Surface [mm^2]
Specimens	452.5	301.6
Components	818.0	740.8

RSs, although the levels are different considering the AB specimens, 56 MPa, and the AB benchmark components, 92.5 MPa. It should be considered that the RSs measured in this study are comparable with values already reported in literature for the same manufacturing process and alloy [55]. From the modelling perspective, the presence of tensile RSs increases the effective load ratio as clearly demonstrated by the Kitagawa diagram reported in Fig. 15b where the El-Haddad model enables to precisely capture the condition of propagation (failure) or non-propagation (run-out) of the AB specimens when calculated according the effective load ratio.

Similarly, the fatigue life predictions performed on the AB specimens (Fig. 16b) and components (Fig. 17b) with the effective load ratio are in excellent agreement with the experimental results, while the simulations performed with the nominal load ratio of R = 0.1 are not conservative, especially in the endurance limit region as also shown by W. Schneller and co-authors in [61].

Moreover, another important factor for the fatigue performance of M benchmark components is the heterogeneity of the RSs measured at different locations (Figs. 11a-b). In all the front surfaces (F1 to F5 in Fig. 11a, Z2 and Z4 in Fig. 11b), we measured compressive RSs down to −150 MPa, while on the two lateral surfaces (Z1 and Z3 in Fig. 11b) tensile RSs were detected. This evidences that it is difficult to precisely associate the failure location with the proper residual stress profile since some failures were detected close to corners (Fig. 7a), where the RSs (due to machining or printing process) vanish. Correspondingly, the life predictions performed on the M benchmark components are particularly meaningful (Fig. 17a) as they clearly demonstrate that the present assessment approach is capable of accounting for the variability associated with the RSs.

It is interesting to notice that for the M cylindrical specimens we measured lower RSs (-76 MPa, see Table 6). On one hand it is expected that the residual stress profile should be almost uniform along the cylindrical specimen surface, on the other hand it indicates that the effective stress ratio at the failure location could be significantly different considering specimens and components. This evidence further suggests that the RSs might provide an additional contribution to the difference in the fatigue performance between M specimens and benchmark components.

7.3. Fracture mechanics-based assessment

The results of the local stress analysis provide a clear indication that an approach based on fracture-mechanics concepts [19] might be more appropriate for the qualification of components manufactured by AM [43,44]. In detail, the adoption of a fracture-based approach enables to take into account the dependence of fatigue properties on defect size, thus allowing to consider the component volume (or size effect) and to clearly establish the lower bound of fatigue properties by adopting an upper bound of the defect size. The effect of the RSs, which is relevant for the AM materials such as Al-Si-Mg and modern Al-based alloys [102] that are subjected to ageing treatments not able to completely relieve RSs, can be easily determined by superimposing the RSs and the stresses from the external loadings (the superposition works only until the maximum stress is lower than material yield limit and assumptions of

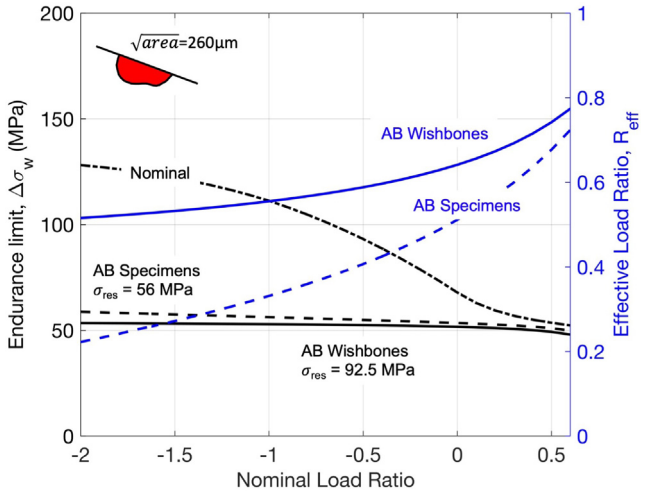

Fig. 20. Effect of the superficial RSs on the endurance limits of AB specimens and AB benchmark components.

elastic-shakedown have to be adopted exceeding this limit [58,103,104]).

If we consider the average surface defect detected on AB specimens and components ($\sqrt{area}$=260μm) and the RSs at P2 and P3 locations, the estimated fatigue limit for different load ratios is plotted in Fig. 20 with and without (nominal) RSs comparing the result for specimens. It can be seen how the fatigue strength is strongly affected by the RSs and how the effective stress ratio R_{eff} is different from the applied load ratio R_L. In fact, due to the high level of tensile RSs, for both the AB specimens and AB benchmark components the effective load (stress) ratio is always positive even though the nominal load ratio $R_L = -2$. If the average residual stress of AB specimens was considered, then the strength would be almost the same: this is due to the flattening of ΔK_{th} curve for high stress ratios and it explains completely the overlap between S-N diagrams of AB specimens and components. It is also interesting to observe that fatigue strength predictions on AB specimens and components were quite good considering the RSs at the defect location (at the surface). Once the fatigue limit is determined, then a log–log linear diagram properly describes well the fatigue life in terms of the driving force [90,105]. Along the same trend, fatigue life of the AB benchmark components does not depend very much on the RSs deeper than 0.5 mm and the simple constant stress profile provides good results [106].

If fracture mechanics-based fatigue assessment can overcome the problems in the transferability of the S-N curves derived from specimens printed with components, on the other side it is clear that it requires an additional effort in terms of experiments for: a) analysing fatigue specimens for determining the size of inhomogeneities at the fracture origin; b) determining crack growth rates and thresholds; c) the RSs on specimens and components (if the thermal treatment does not reach conditions of full relieve of RSs due to manufacturing). In particular, the crack growth experiments require special attention since the fracture properties have to be measured under specific load ratio and this can be accomplished only by testing stress-relieved specimens (or specimens whose location on the built plate minimises the RSs).

8. Conclusions

The present study addressed the manufacturing, characterization and fatigue assessment of AM demonstrators produced by the L-PBF process with the final aim to verify the applicability of the concepts contained in ECSS standards for the qualification of AM components.

To this aim four builds of AlSi10Mg specimen and components were manufactured to: (i) determine the fatigue curves for both AB and M conditions; (ii) measure the fatigue crack growth rate; (iii) test under fatigue a benchmark component used as a reference for the validation of the fatigue assessment procedure; (iv) perform a detailed investigation of experimental test data (fractographies, RSs) to support a detailed fatigue analysis.

The following conclusions are drawn:

- The transferability of fatigue performances from AM specimens to components can be accomplished only with a fracture-based fatigue assessment due to the size effect of the defect distribution and the heterogeneity of the RSs;
- The fatigue performances of AB specimens are comparable with those of the AB demonstrators, while a significant difference is observed for the M conditions;
- The fatigue assessments based on the fracture mechanics are in good agreement with the experimental fatigue performances of both specimens and demonstrators in AB and M conditions, because it allows the designer to properly consider the defect dimension (through *extreme value* statistics) and the residual stress profile (or to consider a conservative scenario for the assessment);
- A fracture mechanics-based fatigue assessment requires a precise measurement of material crack growth rates and thresholds, together with residual stresses on specimens and components.

9. Data Availability

All the data of this benchmark test campaign are available through the *Supplementary Material* of this manuscript.

Declaration of Competing Interest

The authors declare that they have no known competing financial interests or personal relationships that could have appeared to influence the work reported in this paper.

Table 12
Residual stress measurements for M benchmark component BM2-243, Side 1.

		Z1		Z2		Z3			Z4		Z5	
		Point 1	Point 2	Point 1	Point 2	Point 1	Point 2	Point 3	Point 1	Point 2	Point 1	Point 2
σ_{11}	(MPa)	−122	−120.8	−122.8	−126.3	−104.7	−95.4	−101.9	−122.3	−115.3	−113.5	−111.1
SD	(MPa)	13.6	11.7	8.4	7.9	7.8	7.4	7.6	8.1	8	11.1	11.8
σ_{22}	(MPa)	−71.6	−114.5	−107	−103.7	−84.5	−80.6	−77.1	−100.7	−100.2	−106.5	−80.5
SD	(MPa)	13.7	11.7	9.4	7.9	9.4	9	9.3	8.1	8	11.1	11.8
σ_{12}	(MPa)	−25.6	−4.1	−11.3	−14.8	−13.4	−1.4	6.2	17.3	14.5	7.2	−1.2
SD	(MPa)	11.9	10.2	7.4	6.9	7.1	6.7	7	7	7	9.6	10.2

Table 13
Residual stress measurements for M benchmark component BM2-243, Side 2.

		Z1		Z2		Z3			Z4		Z5	
		Point 1	Point 2	Point 1	Point 2	Point 1	Point 2	Point 3	Point 1	Point 2	Point 1	Point 2
σ_{11}	(MPa)	−121	−123.8	−125.7	−121.3	−109.7	−101.7	−107.5	−117.9	−116.8	−127	−126.1
SD	(MPa)	9.8	9.1	8	8.1	7.5	7.9	7.6	8.1	8.2	8	7.8
σ_{22}	(MPa)	−106.2	−99.5	−124.1	−114.7	−127.9	−133.5	−137.5	−120.8	−123.6	−133.7	−125.5
SD	(MPa)	9.8	9.1	8	8.1	9.2	9.5	9.3	8.1	8.2	8	7.8
σ_{12}	(MPa)	−14.6	26.8	9.8	8.6	2.4	0	−99.5	−18.5	27.7	9.1	8
SD	(MPa)	8.6	8	6.9	7.1	6.9	7.2	7	7.1	7.1	7	6.8

Table 14
Residual stress measurements for M benchmark component BM3-242, Side 1.

		Z1		Z2		Z3			Z4		Z5	
		Point 1	Point 2	Point 1	Point 2	Point 1	Point 2	Point 3	Point 1	Point 2	Point 1	Point 2
σ_{11}	(MPa)	−110.4	−106.8	−99.9	−98.4	−118.5	−110.4	−110.4	−87.8	−115.7	−93.6	−93.6
SD	(MPa)	13.2	14.4	6.8	6.9	10.1	10.1	10.1	6.5	9.8	10.1	10.1
σ_{22}	(MPa)	−113.8	−50.9	−119.5	−110.3	−131.1	−129.3	−123.4	−103.7	−140.8	−106.7	−106.7
SD	(MPa)	13.2	14.4	6.9	6.9	12.3	12.2	12.3	6.5	10.4	10.1	10.1
σ_{12}	(MPa)	−19.9	−41.6	−9.3	−13.8	−12	−7.8	0.8	7.4	3.5	3.3	3.3
SD	(MPa)	11.5	12.5	6	6	9.2	9.2	9.2	5.7	9.1	8.8	8.8

Table 15
Residual stress measurements for M benchmark component BM3-242, Side 2.

		Z1		Z2		Z3			Z4		Z5	
		Point 1	Point 2	Point 1	Point 2	Point 1	Point 2	Point 3	Point 1	Point 2	Point 1	Point 2
σ_{11}	(MPa)	−118.6	−114.9	−108.4	−110.3	−116.5	−108.8	−127.9	−115.4	−103.9	−118.9	−114
SD	(MPa)	12.2	12.9	10.2	10.2	10.3	10.4	15	10.4	10.4	13.6	15
σ_{22}	(MPa)	−114.9	−110.1	−111.8	−109.8	−128.7	−127.3	−204.2	−103.1	−100.7	−115.8	−144.6
SD	(MPa)	12.2	12.9	10.2	10.2	12.6	12.7	18.3	10.5	10.4	13.6	15
σ_{12}	(MPa)	−1.8	−3.7	−12	−15.8	−12	−8	31.7	12.9	9.3	14.6	20.8
SD	(MPa)	10.6	11.2	8.9	8.9	9.5	9.5	13.8	9.1	9.1	11.8	13

Table 16
Residual stress measurements on the cut M benchmark component.

		Z1			Z2		Z3			Z4	
		Point 1	Point 2	Point 3	Point 1	Point 2	Point 1	Point 2	Point 3	Point 1	Point 2
σ_{11}	(MPa)	17.8	28.1	5.9	-87.7	-70.6	20	58	19.2	-43.8	-54.6
SD	(MPa)	15.6	15.8	15.7	14.9	15.2	15.3	16.3	15.6	15.7	15.2
σ_{22}	(MPa)	46	48.9	38.2	-79.5	-34.8	100.2	119.5	76.4	-18.2	-58.4
SD	(MPa)	15.6	15.4	15.9	14.9	15.4	15.7	16.4	15.6	16.2	16
σ_{12}	(MPa)	9.9	16.6	1.4	13.1	4.9	1.6	-5.5	-2.8	-24.1	-16.8
SD	(MPa)	14	14	14	13.2	13.6	13.8	14.3	13.8	14	13.5

Table 17
Residual stress measurements on the cut AB benchmark component.

		Z1			Z2		Z3			Z4	
		Point 1	Point 2	Point 3	Point 1	Point 2	Point 1	Point 2	Point 3	Point 1	Point 2
σ_{11}	(MPa)	76.5	94	81.8	66.7	66.8	63.4	82.6	70.2	70.3	62.5
SD	(MPa)	22.9	23.9	23.1	23.8	24.4	23	22.7	22.9	22.4	22.6
σ_{22}	(MPa)	119.9	137	127.2	136	90.3	84.9	91.8	65.4	82.5	138.3
SD	(MPa)	22.6	24.4	25.7	25.5	26.1	23.5	23.4	23.8	22.4	23.9
σ_{12}	(MPa)	−3.3	-11.2	-9.9	-4.3	-9.1	3.7	-7	-17.8	-5.9	-31.1
SD	(MPa)	19.8	20	20.8	21.2	22	19.9	19.7	20	19.5	20.2

Acknowledgements

The present work was carried out within a call-off order of ESA's "Space Additive Manufacturing Benchmarking Center", contract number 4000120221-17- NL-LvH , hosted by the MTC in Coventry. The consortium was composed of the Manufacturing Technology Center (MTC), Politecnico di Milano (Polimi), and the European Space Agency (ESA/ESTEC). The MTC managed the contract from the industrial side and produced under well-controlled conditions the investigated specimens and benchmark components and carried out the necessary post-machining and metrology operations. Polimi carried out material testing, fractographies, analyses, fracture mechanics calculations and assessment. ESA/ESTEC performed complementary materials tests (XRD, roughness) and fatigue tests on the benchmark components. Italian authors acknowledge support provided by MIUR Italian Ministry of Education, University

Table 18
Roughness measurements for the AB cylindrical specimens.

Specimen Number	Stylus R_t (μm)	Stylus R_v (μm)	Stylus $\sqrt{area}$ (μm)
FN1-245	131	79	230
FN2-245	156	109	315
FN3-245	135	70	226
FN4-245	129	74	184
FN5-245	112	68	130
FN7-245	160	100	232
FN3-243	122	77	223
FN4-243	161	119	204
FN5-243	127	71	100
FN6-243	140	105	105
FN7-243	120	80	257

Table 19
Roughness measurements for the AB benchmark components.

Specimen Number	Stylus R_t (μm)	Stylus R_v (μm)	Confocal microscope R_v (μm)	Confocal microscope $\sqrt{area}$ (μm)
BN2-242	120	63	97	217
BN4-242	163	109	75	207
BN1-243	101	58	117	142
BN2-243	136	79	119	177
BN3-243	132	80	73	212
BN4-243	122	81	-	314
	130	70	-	240
BN2-244	153	92	76	167
	181	129	115	188
BN1-245	126	86	97	253
BN2-245	136	75	-	276
BN3-245	106	62	-	165
	113	63	-	238
BN4-245	159	73	-	245

Table 20
Surface roughness measurements (multiline method) for the AB benchmark components near the fracture surface with corresponding failure location.

Specimen Number	R_a (μm)	R_t (μm)	R_v (μm)
BN1-243 (A)	20 ± 4.6	140 ± 31.2	68.7 ± 24.1
BN1-243 (B)	19.0 ± 2.9	126.5 ± 23.8	62.1 ± 19.9
BN2-242 (A)	18.7 ± 3.5	120 ± 25.2	63.4 ± 17
BN2-243 (C)	22.8 ± 4.5	155.4 ± 32.9	73.4 ± 22.7
BN2-244 (A)	18.2 ± 4.3	136 ± 36	67.4 ± 23.9
BN2-244 (B)	17.5 ± 2.2	115.7 ± 15.5	53.2 ± 8.6
BN2-244 (B′)	16.4 ± 3.3	104.8 ± 23	50 ± 13.1
BN3-242 (C′)	14.9 ± 2.9	93.75±24.95	53.18±22.95
BN3-242 (D′)	14.9 ± 2.9	93.8 ± 25	53.2 ± 23
BN3-243 (C)	18.3 ± 3.3	122.5 ± 252	65.9 ± 17.8
BN4-242 (C)	20.7 ± 3.9	123.9 ± 25	52.4 ± 10.1
BN4-242 (D)	17.8 ± 3.1	106.4 ± 20.2	51.5 ± 11.7
BN1-245 (B)	14.8 ± 2.3	84.1 ± 12.2	46.9 ± 11.7
BN1-245 (C)	19.1 ± 3.3	119.5 ± 23.8	61.8 ± 17.6
BN3-245 (C)	15.2 ± 2.7	89.9 ± 13.1	43.4 ± 11.3
BN3-245 (D)	17.2 ± 2.8	107.8 ± 19.7	61.4 ± 18
BN3-245 (C')	22.4 ± 3.8	137.8 ± 23	62.8 ± 16.9
BN1-244 (C)	23.2 ± 4.5	152.3 ± 25.4	70.6 ± 14.2
BN4-243(B′)	21.5 ± 4.2	140.3 ± 29.7	65.2 ± 25.1
BN4-243(C′)	20.9 ± 4.2	137.6 ± 24.2	63.3 ± 16.2
BN4-243(C)	20.4 ± 3.5	133.5 ± 26.8	67.5 ± 19.6
BN2-245 (C′)	20.9 ± 2.9	138 ± 22.3	75.6 ± 16.8
BN2-245 (D′)	16.1 ± 2.5	100.7 ± 19.1	52.9 ± 15.7
BN4-245 (C)	21.1 ± 4.0	137.8 ± 24	61.8 ± 13
BN4-245 (D)	16.9 ± 2.2	112.7 ± 22.6	58.4 ± 21.7

and Research through the Project "Department of Excellence LIS4.0 - Lightweight and Smart Structures for Industry 4.0".

Appendix A

A.1. Residual stress measurements on Machined benchmark components

Tables 12–17.

A.2. Surface roughness measurements and $\sqrt{area}$ of specimens and components

Tables 18–20.

Appendix B. Supplementary material

Supplementary data associated with this article can be found, in the online version, at https://doi.org/10.1016/j.matdes.2022.110713.

References

[1] N. Guo, M.C. Leu, Additive manufacturing: technology, applications and research needs, Front. Mech. Eng. 8 (3) (2013) 215–243.
[2] W.E. Frazier, Metal additive manufacturing: A review (Apr 2014). doi:10.1007/s11665-014-0958-z.
[3] S.L. Sing, J. An, W.Y. Yeong, F.E. Wiria, Laser and electron-beam powder-bed additive manufacturing of metallic implants: A review on processes, materials and designs, J. Orthop. Res. 34 (3) (2016) 369–385, https://doi.org/10.1002/jor.23075.
[4] A. Taşdemir, S. Nohut, An overview of wire arc additive manufacturing (WAAM) in shipbuilding industry, Ships and Offshore Structures (2020) 1–18, https://doi.org/10.1080/17445302.2020.1786232.
[5] A. Gisario, M. Kazarian, F. Martina, M. Mehrpouya, Metal additive manufacturing in the commercial aviation industry: A review (oct 2019). doi:10.1016/j.jmsy.2019.08.005.
[6] A. Uriondo, M. Esperon-Miguez, S. Perinpanayagam, The present and future of additive manufacturing in the aerospace sector: A review of important aspects, Proc. Inst. Mech. Eng., Part G: J. Aerospace Eng. 229 (11) (2015) 2132–2147, https://doi.org/10.1177/0954410014568797.
[7] L. Nickels, AM and aerospace: An ideal combination, Met. Powder Rep. 70 (6) (2015) 300–303, https://doi.org/10.1016/j.mprp.2015.06.005.
[8] R. Liu, Z. Wang, T. Sparks, F. Liou, J. Newkirk, Aerospace applications of laser additive manufacturing, in: Laser Additive Manufacturing: Materials, Design, Technologies, and Applications, Elsevier Inc., 2017, pp. 351–371. doi:10.1016/B978-0-08-100433-3.00013-0.
[9] S.C. Joshi, A.A. Sheikh, 3D printing in aerospace and its long-term sustainability, Virtual and Physical Prototyping 10 (4) (2015) 175–185, https://doi.org/10.1080/17452759.2015.1111519.
[10] D.E. Cooper, M. Stanford, K.A. Kibble, G.J. Gibbons, Additive Manufacturing for product improvement at Red Bull Technology, Mater. Des. 41 (2012) 226–230, https://doi.org/10.1016/j.matdes.2012.05.017.
[11] F. Cucinotta, M. Raffaele, F. Salmeri, A Topology Optimization of a Motorsport Safety Device (2020) 400–409.
[12] B. Blakey-Milner, P. Gradl, G. Snedden, M. Brooks, J. Pitot, E. Lopez, M. Leary, F. Berto, A. du Plessis, Metal additive manufacturing in aerospace: A review, Materials & Design 209 (2021) 110008.
[13] Airbus website. https://www.airbus.com/space/telecommunications-satellites/oneweb-satellites-connection-for-people-all-over-the-globe.html.
[14] Spacenews website. https://spacenews.com/oneweb-slashes-size-of-future-satellite-constellation/.
[15] A. Yadollahi, N. Shamsaei, Additive manufacturing of fatigue resistant materials: Challenges and opportunities, Int. J. Fatigue 98 (2017) 14–31, https://doi.org/10.1016/j.ijfatigue.2017.01.001.
[16] A. Mostafaei, C. Zhao, Y. He, S.R. Ghiaasiaan, B. Shi, S. Shao, N. Shamsaei, Z. Wu, N. Kouraytem, T. Sun, et al., Defects and anomalies in powder bed fusion metal additive manufacturing, Curr. Opin. Solid State Mater. Sci. 26 (2) (2022) 100974.
[17] N. Sanaei, A. Fatemi, Defects in additive manufactured metals and their effect on fatigue performance: A state-of-the-art review, Prog. Mater Sci. 117 (2021) 100724, https://doi.org/10.1016/J.PMATSCI.2020.100724.
[18] A. du Plessis, S. Beretta, Killer notches: The effect of as-built surface roughness on fatigue failure in AlSi10Mg produced by laser powder bed fusion, Additive Manufacturing 35 (2020) 101424, https://doi.org/10.1016/j.addma.2020.101424.
[19] S. Romano, A. Brückner-Foit, A. Brand ao, J. Gumpinger, T. Ghidini, S. Beretta, Fatigue properties of AlSi10Mg obtained by additive manufacturing: Defect-

based modelling and prediction of fatigue strength, Engineering Fracture Mechanics 187 (2018) 165–189. doi:10.1016/j.engfracmech.2017.11.002.
[20] J.J. Lewandowski, M. Seifi, Metal additive manufacturing: a review of mechanical properties, Annual review of materials research 46 (2016) 151–186.
[21] W. Tillmann, C. Schaak, J. Nellesen, M. Schaper, M.E. Aydinöz, K.P. Hoyer, Hot isostatic pressing of IN718 components manufactured by selective laser melting, Additive Manufacturing 13 (2017) 93–102, https://doi.org/10.1016/j.addma.2016.11.006.
[22] J. Benzing, N. Hrabe, T. Quinn, R. White, R. Rentz, M. Ahlfors, Hot isostatic pressing (HIP) to achieve isotropic microstructure and retain as-built strength in an additive manufacturing titanium alloy (Ti-6Al-4V), Mater. Lett. 257 (2019) 126690, https://doi.org/10.1016/j.matlet.2019.126690.
[23] A. Du Plessis, E. Macdonald, Hot isostatic pressing in metal additive manufacturing: X-ray tomography reveals details of pore closure, Additive Manufacturing 34 (2020) 101191.
[24] E. Yasa, J. Deckers, J.P. Kruth, The investigation of the influence of laser re-melting on density, surface quality and microstructure of selective laser melting parts, Rapid Prototyping Journal 17 (5) (2011) 312–327, https://doi.org/10.1108/13552541111156450.
[25] S. Bagherifard, N. Beretta, S. Monti, M. Riccio, M. Bandini, M. Guagliano, On the fatigue strength enhancement of additive manufactured AlSi10Mg parts by mechanical and thermal post-processing, Materials & Design 145 (2018) 28–41, https://doi.org/10.1016/J.MATDES.2018.02.055.
[26] S.M. Ahmadi, R. Kumar, E.V. Borisov, R. Petrov, S. Leeflang, Y. Li, N. Tümer, R. Huizenga, C. Ayas, A.A. Zadpoor, V.A. Popovich, From microstructural design to surface engineering: A tailored approach for improving fatigue life of additively manufactured meta-biomaterials, Acta Biomater. 83 (2019) 153–166, https://doi.org/10.1016/J.ACTBIO.2018.10.043.
[27] E. Maleki, S. Bagherifard, M. Bandini, M. Guagliano, Surface post-treatments for metal additive manufacturing: Progress, challenges, and opportunities, Additive Manufacturing 37 (2021) 101619.
[28] S. Beretta, S. Romano, A comparison of fatigue strength sensitivity to defects for materials manufactured by am or traditional processes, International Journal of Fatigue 94 (2017) 178–191, fatigue and Fracture Behavior of Additive Manufactured Parts. doi: 10.1016/j.ijfatigue.2016.06.020.
[29] U. Zerbst, G. Bruno, J.-Y. Buffiere, T. Wegener, T. Niendorf, T. Wu, X. Zhang, N. Kashaev, G. Meneghetti, N. Hrabe, Damage tolerant design of additively manufactured metallic components subjected to cyclic loading: State of the art and challenges, Progress in materials science 121 (2021).
[30] P. Mercelis, J.P. Kruth, Residual stresses in selective laser sintering and selective laser melting, Rapid Prototyping Journal 12 (5) (2006) 254–265, https://doi.org/10.1108/13552540610707013.
[31] T. DebRoy, H.L. Wei, J.S. Zuback, T. Mukherjee, J.W. Elmer, J.O. Milewski, A.M. Beese, A. Wilson-Heid, A. De, W. Zhang, Additive manufacturing of metallic components – Process, structure and properties, Prog. Mater Sci. 92 (2018) 112–224, https://doi.org/10.1016/j.pmatsci.2017.10.001.
[32] K. Carpenter, A. Tabei, On Residual Stress Development, Prevention, and Compensation in Metal Additive Manufacturing, Materials 2020, Vol. 13, Page 255 13 (2) (2020) 255. doi:10.3390/MA13020255.
[33] N.T. Aboulkhair, I. Maskery, C. Tuck, I.A. Ashcroft, N.M. Everitt, Improving the fatigue behaviour of a selectively laser melted aluminium alloy: Influence of heat treatment and surface quality, Mater. Des. 104 (2016) 174–182, https://doi.org/10.1016/j.matdes.2016.05.041.
[34] P. Edwards, A. O'Conner, M. Ramulu, Electron Beam Additive Manufacturing of Titanium Components: Properties and Performance, Journal of Manufacturing Science and Engineering 135 (6) (dec 2013). doi:10.1115/1.4025773.
[35] S. Leuders, S. Meiners, L. Wu, A. Taube, T. Tröster, T. Niendorf, Structural components manufactured by Selective Laser Melting and Investment Casting—Impact of the process route on the damage mechanism under cyclic loading, J. Mater. Process. Technol. 248 (2017) 130–142, https://doi.org/10.1016/J.JMATPROTEC.2017.04.026.
[36] R. Molaei, A. Fatemi, N. Sanaei, J. Pegues, N. Shamsaei, S. Shao, P. Li, D.H. Warner, N. Phan, Fatigue of additive manufactured Ti-6Al-4V, Part II: The relationship between microstructure, material cyclic properties, and component performance, Int. J. Fatigue 132 (2020) 105363, https://doi.org/10.1016/j.ijfatigue.2019.105363.
[37] P. Li, D.H. Warner, N. Phan, Predicting the fatigue performance of an additively manufactured Ti-6Al-4V component from witness coupon behavior, Additive Manufacturing 35 (2020) 101230, https://doi.org/10.1016/J.ADDMA.2020.101230.
[38] K. Schnabel, J. Baumgartner, B. Möller, M. Scurria, Fatigue assessment of additively manufactured AlSi10Mg structures using effective stress concepts based on the critical distance approach, Welding in the World 65 (11) (2021) 2119–2133, https://doi.org/10.1007/S40194-021-01153-9/FIGURES/18.
[39] S. Romano, A. Brand ao, J. Gumpinger, M. Gschweitl, S. Beretta, Qualification of AM parts: Extreme value statistics applied to tomographic measurements, Materials and Design 131 (2017) 32–48. doi:10.1016/j.matdes.2017.05.091.
[40] A. du Plessis, S.G. le Roux, Standardized x-ray tomography testing of additively manufactured parts: A round robin test, Additive Manufacturing 24 (2018) 125–136.
[41] S. Senck, M. Happl, M. Reiter, M. Scheerer, M. Kendel, J. Glinz, J. Kastner, Additive manufacturing and non-destructive testing of topology-optimised aluminium components, Nondestruct. Test. Eval. 35 (3) (2020) 315–327.
[42] M. Seifi, M. Gorelik, J. Waller, N. Hrabe, N. Shamsaei, S. Daniewicz, J.J. Lewandowski, Progress Towards Metal Additive Manufacturing Standardization to Support Qualification and Certification, JOM 2017 69:3 69 (3) (2017) 439–455. doi:10.1007/S11837-017-2265-2.
[43] M. Gorelik, Additive manufacturing in the context of structural integrity, Int. J. Fatigue 94 (2017) 168–177, https://doi.org/10.1016/J.IJFATIGUE.2016.07.005.
[44] J. Mochache, R.M. Taylor, A review of fatigue and damage tolerance life prediction methodologies toward certification of additively manufactured metallic principal structural elements, in: AIAA Scitech 2021 Forum, 2021, p. 1509.
[45] E. Beevers, A.D. Brand ao, J. Gumpinger, M. Gschweitl, C. Seyfert, P. Hofbauer, T. Rohr, T. Ghidini, Fatigue properties and material characteristics of additively manufactured AlSi10Mg – Effect of the contour parameter on the microstructure, density, residual stress, roughness and mechanical properties, Int. J. Fatigue 117 (2018) 148–162. doi:10.1016/j.ijfatigue.2018.08.023.
[46] N.T. Aboulkhair, M. Simonelli, L. Parry, I. Ashcroft, C. Tuck, R. Hague, 3D printing of Aluminium alloys: Additive Manufacturing of Aluminium alloys using selective laser melting (dec 2019). doi:10.1016/j.pmatsci.2019.100578.
[47] F. Trevisan, F. Calignano, M. Lorusso, J. Pakkanen, A. Aversa, E. Ambrosio, M. Lombardi, P. Fino, D. Manfredi, On the Selective Laser Melting (SLM) of the AlSi10Mg Alloy: Process, Microstructure, and Mechanical Properties, Materials 10 (1) (2017) 76, https://doi.org/10.3390/ma10010076.
[48] G.E. Totten (Ed.), ASM Handbook Volume 4E: Heat Treating of Nonferrous Alloys, ASM International, 2016.
[49] L. Lam, D. Zhang, Z. Liu, C. Chua, Phase analysis and microstructure characterisation of AlSi10Mg parts produced by Selective Laser Melting, Virtual and Physical Prototyping 10 (4) (2015) 207–215, https://doi.org/10.1080/17452759.2015.1110868.
[50] D. Manfredi, F. Calignano, M. Krishnan, R. Canali, E. Ambrosio, E. Atzeni, From Powders to Dense Metal Parts: Characterization of a Commercial AlSiMg Alloy Processed through Direct Metal Laser Sintering, Materials 6 (3) (2013) 856–869, https://doi.org/10.3390/ma6030856.
[51] L. Thijs, K. Kempen, J.P. Kruth, J. Van Humbeeck, Fine-structured aluminium products with controllable texture by selective laser melting of pre-alloyed AlSi10Mg powder, Acta Mater. 61 (5) (2013) 1809–1819, https://doi.org/10.1016/j.actamat.2012.11.052.
[52] E8/E8M-21 Standard Test Methods for Tension Testing of Metallic Materials (2021).
[53] ASTM, E739-10 Standard Practice for Statistical Analysis of Linear or Linearized Stress-Life (S-N) and Strain-Life (ϵ-N) Fatigue Data, Tech. rep., American Sosciety for Testing and Materials, West Conshohocken, PA (2015). doi:https://doi.org/10.1520/E0739-10R15.
[54] W.J. Dixon, The up-and-down method for small samples, Journal of the American Statistical Association 60 (312) (1965) 967–978.
[55] A. Salmi, E. Atzeni, Residual stress analysis of thin AlSi10Mg parts produced by Laser Powder Bed Fusion, Virtual and Physical Prototyping 15 (1) (2020) 49–61, https://doi.org/10.1080/17452759.2019.1650237.
[56] E. Capello, Residual stresses in turning: Part i: Influence of process parameters, Journal of materials processing technology 160 (2) (2005) 221–228.
[57] F. Sausto, S. Beretta, P. Carrion, N. Shamsaei, Fatigue failure mechanisms for AlSi10Mg manufactured by L-PBF under axial and torsional loads: the role of defects and residual stresses, Int. J. Fatigue (accepted manuscript) (2022).
[58] S. Beretta, M. Gargourimotlagh, S. Foletti, A. du Plessis, M. Riccio, Fatigue strength assessment of "as built" AlSi10Mg manufactured by SLM with different build orientations, Int. J. Fatigue 139 (2020) 105737, https://doi.org/10.1016/j.ijfatigue.2020.105737.
[59] L. Wang, X. Jiang, Y. Zhu, X. Zhu, J. Sun, B. Yan, An approach to predict the residual stress and distortion during the selective laser melting of AlSi10Mg parts, The International Journal of Advanced Manufacturing Technology 97 (9–12) (2018) 3535–3546.
[60] A. Salmi, E. Atzeni, History of residual stresses during the production phases of AlSi10Mg parts processed by powder bed additive manufacturing technology, Virtual and Physical Prototyping 12 (2) (2017) 153–160, https://doi.org/10.1080/17452759.2017.1310439.
[61] W. Schneller, M. Leitner, S. Pomberger, F. Grün, S. Leuders, T. Pfeifer, O. Jantschner, Fatigue strength assessment of additively manufactured metallic structures considering bulk and surface layer characteristics, Additive Manufacturing 40 (2021) 101930, https://doi.org/10.1016/j.addma.2021.101930.
[62] Y. Murakami, Metal fatigue: effects of small defects and nonmetallic inclusions, Academic Press, 2019.
[63] S. Beretta, Y. Murakami, Statistical analysis of defects for fatigue strength prediction and quality control of materials, Fatigue Fract. Eng. Mater. Struct. 21 (9) (1998) 1049–1065, https://doi.org/10.1046/j.1460-2695.1998.00104.x.
[64] G. Schweiger, K. Heckel, Size effect in randomly loaded specimens, Int. J. Fatigue 8 (4) (1986) 231–234, https://doi.org/10.1016/0142-1123(86)90026-5.
[65] H. Bomas, T. Linkewitz, P. Mayr, Application of a weakest-link concept to the fatigue limit of the bearing steel SAE 52100 in a bainitic condition, Fatigue & Fracture of Engineering Materials & Structures 22 (9) (1999) 733–741, https://doi.org/10.1046/J.1460-2695.1999.T01-1-00211.X.

[66] M. Shirani, G. Härkegård, Fatigue life distribution and size effect in ductile cast iron for wind turbine components, Eng. Fail. Anal. 18 (1) (2011) 12–24, https://doi.org/10.1016/J.ENGFAILANAL.2010.07.001.
[67] D.S. Paolino, Very high cycle fatigue life and critical defect size: Modeling of statistical size effects, Fatigue & Fracture of Engineering Materials & Structures 44 (5) (2021) 1209–1224, https://doi.org/10.1111/FFE.13424.
[68] D. El Khoukhi, F. Morel, N. Saintier, D. Bellett, P. Osmond, V.D. Le, Probabilistic modeling of the size effect and scatter in High Cycle Fatigue using a Monte-Carlo approach: Role of the defect population in cast aluminum alloys, Int. J. Fatigue 147 (2021) 106177, https://doi.org/10.1016/j.ijfatigue.2021.106177.
[69] J. Gockel, L. Sheridan, B. Koerper, B. Whip, The influence of additive manufacturing processing parameters on surface roughness and fatigue life, Int. J. Fatigue 124 (2019) 380–388, https://doi.org/10.1016/j.ijfatigue.2019.03.025.
[70] S. Lee, B. Rasoolian, D.F. Silva, J.W. Pegues, N. Shamsaei, Surface roughness parameter and modeling for fatigue behavior of additive manufactured parts: A non-destructive data-driven approach, Additive Manufacturing (2021) 102094.
[71] T. Persenot, A. Burr, R. Dendievel, J.Y. Buffière, E. Maire, J. Lachambre, G. Martin, Fatigue performances of chemically etched thin struts built by selective electron beam melting: Experiments and predictions, Materialia 9 (2020), https://doi.org/10.1016/j.mtla.2020.100589.
[72] L. Barricelli, S. Beretta, Analysis of prospective sif and shielding effect for cylindrical rough surfaces obtained by l-pbf, Eng. Fract. Mech. 256 (2021) 107983.
[73] D. Greitemeier, C.D. Donne, F. Syassen, J. Eufinger, T. Melz, Effect of surface roughness on fatigue performance of additive manufactured Ti-6Al-4V, Mater. Sci. Tech. 32 (2015) 629–634.
[74] D. Greitemeier, F. Palm, F. Syassen, T. Melz, Fatigue performance of additive manufactured TiAl6V4 using electron and laser beam melting, Int. J. Fatigue 94 (2017) 211–217.
[75] H. Masuo, Y. Tanaka, S. Morokoshi, T. Uchida, Y. Yamamoto, Y. Murakami, Influence of defects, surface roughness and HIP on the fatigue strength of Ti-6Al-4V manufactured by additive manufacturing, Int. J. Fatigue 117 (2018) 163–179.
[76] M. Nakatani, H. Masuo, Y. Tanaka, Y. Murakami, Effect of Surface Roughness on Fatigue Strength of Ti-6Al-4V Alloy Manufactured by Additive Manufacturing, Procedia Structural Integrity 19 (2019) 294–301, https://doi.org/10.1016/j.prostr.2019.12.032.
[77] N. Dowling, Mechanical behaviour of materials. engineering methods for deformation, fracture, and fatigue. fourth (2013).
[78] X. Wang, S.B. Lambert, Stress intensity factors for low aspect ratio semi-elliptical surface cracks in finite-thickness plates subjected to nonuniform stresses, Eng. Fract. Mech. 51 (4) (1995) 517–532, https://doi.org/10.1016/0013-7944(94)00311-5.
[79] X. Wang, S. Lambert, Stress intensity factors and weight functions for high aspect ratio semi-elliptical surface cracks in finite-thickness plates, Eng. Fract. Mech. 57 (1) (1997) 13–24, https://doi.org/10.1016/S0013-7944(97)00018-0.
[80] L. Patriarca, M. Filippini, S. Beretta, Short-crack thresholds and propagation in an aisi 4340 steel under the effect of sp residual stresses, Fatigue & Fracture of Engineering Materials & Structures 41 (6) (2018) 1275–1290.
[81] ECSS-Q-ST-70-80C, Processing and quality assurance requirements for metallic powder bed fusion technologies for space applications, European Space Agency (July 2021).
[82] S. Romano, S. Miccoli, S. Beretta, A new FE post-processor for probabilistic fatigue assessment in the presence of defects and its application to AM parts, Int. J. Fatigue 125 (2019) 324–341, https://doi.org/10.1016/J.IJFATIGUE.2019.04.008.
[83] A. Fatemi, R. Molaei, S. Sharifimehr, N. Phan, N. Shamsaei, Multiaxial fatigue behavior of wrought and additive manufactured ti-6al-4v including surface finish effect, Int. J. Fatigue 100 (2017) 347–366, https://doi.org/10.1016/j.ijfatigue.2017.03.044.
[84] J.N.D. Ngnekou, Y. Nadot, G. Henaff, J. Nicolai, W.H. Kan, J.M. Cairney, L. Ridosz, Fatigue properties of alsi10mg produced by additive layer manufacturing, Int. J. Fatigue 119 (2019) 160–172.
[85] Z. Wu, S. Wu, J. Bao, W. Qian, S. Karabal, W. Sun, P.J. Withers, The effect of defect population on the anisotropic fatigue resistance of AlSi10Mg alloy fabricated by laser powder bed fusion, Int. J. Fatigue 151 (2021) 106317.
[86] Y. Hu, S. Wu, P. Withers, J. Zhang, H. Bao, Y. Fu, G. Kang, The effect of manufacturing defects on the fatigue life of selective laser melted ti-6al-4v structures, Materials & Design 192 (2020) 108708.
[87] E. Akgun, X. Zhang, T. Lowe, Y. Zhang, M. Doré, Fatigue of laser powder-bed fusion additive manufactured Ti-6Al-4V in presence of process-induced porosity defects, Eng. Fract. Mech. 259 (2022) 108140.
[88] A. Yadollahi, M. Mahtabi, A. Khalili, H. Doude, J. Newman Jr, Fatigue life prediction of additively manufactured material: Effects of surface roughness, defect size, and shape, Fatigue & Fracture of Engineering Materials & Structures 41 (7) (2018) 1602–1614.
[89] K. Solberg, S. Guan, S.M.J. Razavi, T. Welo, K.C. Chan, F. Berto, Fatigue of additively manufactured 316l stainless steel: The influence of porosity and surface roughness, Fatigue & Fracture of Engineering Materials & Structures 42 (9) (2019) 2043–2052.
[90] S. Romano, P. Nezhadfar, N. Shamsaei, M. Seifi, S. Beretta, High cycle fatigue behavior and life prediction for additively manufactured 17–4 ph stainless steel: Effect of sub-surface porosity and surface roughness, Theoret. Appl. Fract. Mech. 106 (2020) 102477.
[91] P. Merot, F. Morel, L.G. Mayorga, E. Pessard, P. Buttin, T. Baffie, Observations on the influence of process and corrosion related defects on the fatigue strength of 316l stainless steel manufactured by laser powder bed fusion (l-pbf), Int. J. Fatigue 155 (2022) 106552.
[92] Y. Yamashita, T. Murakami, R. Mihara, M. Okada, Y. Murakami, Defect analysis and fatigue design basis for ni-based superalloy 718 manufactured by selective laser melting, Int. J. Fatigue 117 (2018) 485–495.
[93] A. Yadollahi, M. Mahtabi, A. Khalili, H. Doude, J. Newman, Fatigue life prediction of additively manufactured material: Effects of surface roughness, defect size, and shape, Fatigue & Fracture of Engineering Materials & Structures 41 (7) (2018) 1602–1614, https://doi.org/10.1111/ffe.12799.
[94] J.-R. Poulin, A. Kreitcberg, P. Terriault, V. Brailovski, Fatigue strength prediction of laser powder bed fusion processed inconel 625 specimens with intentionally-seeded porosity: Feasibility study, Int. J. Fatigue 132 (2020) 105394.
[95] L. Sheridan, J.E. Gockel, O.E. Scott-Emuakpor, Stress-defect-life interactions of fatigued additively manufactured alloy 718, Int. J. Fatigue 143 (2021) 106033.
[96] J. Schijve, Fatigue of structures and materials, Springer Science & Business Media, 2001.
[97] S. Beretta, More than 25 years of Extreme Value Statistics for defects: Fundamentals, historical developments, recent applications, Int. J. Fatigue 151 (2021) 106407, https://doi.org/10.1016/J.IJFATIGUE.2021.106407.
[98] N. Sanaei, A. Fatemi, N. Phan, Defect characteristics and analysis of their variability in metal l-pbf additive manufacturing, Materials & Design 182 (2019) 108091.
[99] J.W. Pegues, S. Shao, N. Shamsaei, N. Sanaei, A. Fatemi, D.H. Warner, P. Li, N. Phan, Fatigue of additive manufactured Ti-6Al-4V, Part I: The effects of powder feedstock, manufacturing, and post-process conditions on the resulting microstructure and defects, Int. J. Fatigue 132 (2020) 105358, https://doi.org/10.1016/J.IJFATIGUE.2019.105358.
[100] V. Sandell, T. Hansson, S. Roychowdhury, T. Månsson, M. Delin, P. Åkerfeldt, M.-L. Antti, Defects in electron beam melted ti-6al-4v: Fatigue life prediction using experimental data and extreme value statistics, Materials 14 (3) (2021) 640.
[101] R.-D. Reiss, M. Thomas, R. Reiss, Statistical analysis of extreme values (1997).
[102] M. Muhammad, P. Nezhadfar, S. Thompson, A. Saharan, N. Phan, N. Shamsaei, A comparative investigation on the microstructure and mechanical properties of additively manufactured aluminum alloys, Int. J. Fatigue 146 (2021) 106165.
[103] W.T. Koiter, General theorems for elastic plastic solids, in: Progress in Solid Mechanics, North Holland Press, 1960, pp. 167–221.
[104] A. Ponter, A general shakedown theorem for elastic/plastic bodies with work hardening, in: 3rd SMiRT Conference London, lASMiRT, 1975, p. L 5/2.
[105] Y. Murakami, T. Takagi, K. Wada, H. Matsunaga, Essential structure of s-n curve: Prediction of fatigue life and fatigue limit of defective materials and nature of scatter, Int. J. Fatigue 146 (2021).
[106] S. Beretta, F. Sausto, C. Tezzele, Fracture-based fatigue life prediction, based on tests results of AlSiMg10 wishbones, with special emphasis on the effect of residual stress, Tech. Rep. n. 1–82/21CR, Politecnico di Milano, Dept. Mechanical Engineering (2021).